

# Topology-Optimized Porous Electrode Architectures for Enhanced Performance in Vanadium Redox Flow Batteries in Flow-Through Cell Designs

Poramet Aiemsathit, Mehrzad Alizadeh, Yossapong Laoonual,  
Patcharawat Charoen-amornkitt,\* Takahiro Suzuki, and Shohji Tsushima

Herein, a comprehensive investigation is presented into the optimization of porous electrode (PE) structures in vanadium redox flow batteries (VRFBs) using topology optimization (TO) to enhance cell performance, particularly in flow-through configurations. This work builds upon prior studies by incorporating a full cell model that accounts for species transport, electrolyte flow, charge transfer, and proton transport within both positive and negative electrodes. PEs are optimized under different depths of discharge (DoD) conditions—5%, 50%, 65%, 90% and 95%—to capture the diverse requirements for reaction kinetics and mass transport under varying reactant concentrations. The optimized structures, featuring interdigitated channels on both electrodes, yield substantial improvements in mass transport

and reaction rates compared to unmodified flow-through and interdigitated flow-field configurations. Performance tests, including polarization curves and charge/discharge characteristics, demonstrate superior current density and electrolyte utilization in the optimized flow-through porous electrode (OFT) designs. Among these, the OFT95% (optimized at 95% DoD) performs exceptionally well under low reactant conditions. Despite minor tradeoffs in hydraulic power loss, the optimized structures maintain competitive round-trip efficiency, showing promise for real-world applications. This study provides critical insights into electrode engineering for VRFBs, contributing to the advancement of sustainable energy storage technologies essential for achieving carbon neutrality.

## 1. Introduction

Global warming has been a growing concern for several decades. Greenhouse gases accumulating in Earth's atmosphere act as heat absorbers, raising the planet's temperature. This increase in temperature affects natural ecosystems, human activity, and resources, leading to potentially catastrophic outcomes. Among these gases, carbon dioxide is the most significant contributor, primarily emitted by key economic sectors such as transportation, industry, and energy production.<sup>[1]</sup> To combat the effects of global warming, conventional fossil fuel energy sources must be replaced with renewable, clean, and sustainable alternatives.<sup>[2]</sup> Renewable energy sources, such as solar, wind, and hydro,

meet the need for clean and sustainable energy. However, their availability is dependent on weather conditions and timing, leading to fluctuations in energy generation. To address this inconsistency, Energy storage systems (ESS) play a crucial role in stabilizing power supply by storing excess energy during periods of surplus. ESS includes various technologies and equipment that store energy for later use. The main methods of energy storage fall into three categories: electrochemical (e.g., batteries, supercapacitors), mechanical (e.g., gravity, kinetic systems), and thermodynamic (e.g., thermal storage, compressed air cycles).<sup>[3]</sup>

Among ESSs, the vanadium redox flow battery (VRFB) stands out for its unique ability to provide energy independently of power and capacity constraints. Also, unlike traditional energy storage methods, such as pumped hydro, which are limited by geographical site conditions and require significant elevation differences for operation, VRFBs can be deployed in a variety of locations without the need for specific topographical features. This independence allows for greater flexibility in system design and scaling. The power and capacity of VRFBs can be adjusted independently, enabling operators to tailor the system to meet specific energy demands without being restricted by physical site limitations. Consequently, VRFBs are particularly advantageous for providing reliable energy during urgent situations and effectively supporting the grid by managing peak loads during periods of high electricity demand.<sup>[4]</sup> However, challenges remain in scaling up VRFBs for effective commercialization, primarily due to performance limitations and high capital costs. The system comprises various components, some of which, like electrolytes,

P. Aiemsathit, P. Charoen-amornkitt  
Electrochemical Energy Storage and Conversion Laboratory  
Department of Mechanical Engineering  
Faculty of Engineering  
King Mongkut's University of Technology Thonburi  
126 Pracha Uthit Road, Bang Mod, Thung Khru, Bangkok 10140, Thailand  
E-mail: patcharawat.cha@kmutt.ac.th  
  
M. Alizadeh, T. Suzuki, S. Tsushima  
Department of Mechanical Engineering  
Graduate School of Engineering  
Osaka University  
2-1 Yamadaoka, Suita, Osaka 565-0871, Japan  
  
Y. Laoonual  
Mobility & Vehicle Technology Research Center  
King Mongkut's University of Technology Thonburi  
126 Pracha Uthit Road, Bang Mod, Thung Khru, Bangkok 10140, Thailand

bipolar plates, and graphite felt electrodes, are particularly expensive but essential for the VRFB's efficient operation.<sup>[5]</sup> To promote renewable energy integration—such as combining VRFBs with solar and wind farms—improving adaptability and cost-effectiveness is crucial. The two main challenges are enhancing battery performance and reducing costs. These objectives can be achieved through performance optimization and minimizing material usage. Improving battery cell performance requires a deep understanding of electrochemical systems to optimize the design of key components.

Over the past few decades, advancements in VRFB components, such as porous electrode (PE),<sup>[6,7]</sup> have contributed to overall performance improvements. Typically, electrodes undergo optimization of both their electrochemical and structural properties through various treatment and modification processes.<sup>[8]</sup> In this regard, our research group, for example, has developed numerical modeling approaches to better interpret cyclic voltamograms by separating faradaic and non-faradaic currents, particularly for porous electrodes.<sup>[9]</sup> Our approach provides a comprehensive understanding of how these modifications fundamentally contribute to cell performance.

Improving cell performance relies heavily on optimizing flow channel or flow field design, which is a key factor in enhancing the mass transport of active species to promote electrochemical reactions within the battery cell. It is noteworthy that mass transport can be enhanced through the design of flow fields on the surface of bipolar plates in flow-by architectures. For example, employing different flow field patterns—such as interdigitated, serpentine, or parallel flow channels—can significantly influence fluid distribution and reactant accessibility. Additionally, integrating the flow field directly into the porous electrode (by machining it onto the electrode itself) can further facilitate the transport of active species into electrochemically active regions, thereby improving overall cell performance. Various flow field architectures have been proposed, many of which have been extensively studied in fuel cells.<sup>[10]</sup> Traditionally, cells have employed a flow-through architecture, where electrolytes are distributed directly to the PE without a flow channel on the bipolar plate. In contrast, the flow-by architecture uses machined flow channels on the bipolar plate-electrode interface to supply electrolytes. Variations in flow channel direction, dimensions, shapes, and baffles significantly impact mass transport behavior. Among the most researched designs are the interdigitated flow field (IFF), serpentine flow field, and spiral flow field.<sup>[11–15]</sup> These designs have gained attention for their ability to enhance uniformity in reactant distribution within the electrodes and reduce overpotential gradients, thus improving overall performance.<sup>[16]</sup> The flow field architecture significantly impacts cell performance by influencing both mass transport and the uniformity of reactant distribution. In particular, the dimensions of the flow field—such as width, depth, and length—play a crucial role in optimizing performance. Guo et al.<sup>[17]</sup> studied the dimensions of IFF and found that width and channel fraction have a substantial effect on the mass transport properties of electrolytes beneath the rib, including pressure drop, uniformity, and overpotential. They concluded that a 2 mm channel width is optimal. A narrower channel width

leads to a higher pressure drop, reduced reaction area due to a shorter convective path, and insufficient reactant supply, all of which result in increased overpotential. Conversely, a wider channel lengthens the convective path, slightly increasing the pressure drop due to flow resistance. However, this also causes a lack of active species in certain areas, leading to a modest rise in overpotential gradients. Additionally, the shape of the flow path within the flow field plays a critical role in influencing reactant mass transport. Even when a battery cell is paired with an optimal flow field architecture and dimensions, the shape can alter how electrolytes reach the PE, affecting electrochemical reaction processes. Akuzum et al.<sup>[12]</sup> explored various nonuniform flow channel depths using both open-ended and closed-ended designs in IFF and parallel flow field. Their findings showed that a gradual electrolyte supply to the PE results in the highest performance by improving penetration depth into the electrode-membrane interface, where electron transfer reactions occur. While flow-by architecture delivers enhanced performance, it requires thicker bipolar plates to incorporate machined flow channels. This added thickness can limit its suitability for high-performance stacks intended for large-scale commercialization.

On the other hand, modifications to the PE have a significant impact on battery performance, as most electrochemical reactions occur at the PE. However, optimizing cell performance through PE modifications requires balancing enhanced mass transport with the availability of specific active areas for electrochemical reactions. Mayrhuber et al.<sup>[6]</sup> investigated the effects of PE perforations and found that these modifications significantly improve cell performance, increasing both peak power and limiting current while slightly reducing porosity. This results in a larger active surface area, leading to higher peak power density. Similarly motivated, one intriguing approach involves machining flow channels directly onto the PE, effectively combining flow-through architecture with integrated flow fields. In this design, electrolytes are guided by the integrated channels, altering mass transport and reactant distribution compared to conventional flow-through designs. This change notably impacts the limiting current, especially when operating at low flow rates. For instance, Bhattacharai et al.<sup>[7]</sup> compared various flow fields integrated into the PE with conventional designs. They found that at low electrolyte flow rates, unmodified PEs led to reactant starvation, resulting in an inability to sustain high current density due to the limiting current. In contrast, modified PEs exhibited a higher specific surface area compared to unmodified ones. Although machining the PE leads to some material loss, the tradeoff is worthwhile, as the slight reduction in electronic conductivity is compensated by a significant increase in the limiting current. Similar modifications can also be found in fuel cell applications. Watanabe et al.<sup>[18]</sup> developed a novel gas diffusion layer (GDL) integrated with interdigitated flow channels using stamping and molding methods, allowing for mass production of this design. This design addresses water blockage at the separator and interdigitated channel-GDL interfaces under rib areas. The interdigitated channels enhance water removal through forced convection of O<sub>2</sub>, significantly reducing contact resistance and increasing voltage at specified current densities. Additionally, Inoue et al.<sup>[19]</sup> studied

the impact of interdigitated flow channels on flat metal separators under extreme conditions. They found that conventional interdigitated channels often experience voltage drops at high relative humidity, whereas GDLs with interdigitated flow channels maintain stability.

Unfortunately, these modifications and improvements, including both flow field design and electrode structural modifications, often rely on intuition-based approaches, leading to inefficient use of limited resources in terms of both materials and time. To address this issue, mathematical optimization techniques are commonly employed in engineering to develop effective systems that meet specific objectives. A notable trend in electrode optimization is the use of TO to identify optimal structures.<sup>[20]</sup> TO originated in structural design<sup>[21,22]</sup> and has since been applied in various fields, including thermo-fluid applications,<sup>[23–25]</sup> as well as electrochemical systems like diffusion-reaction systems,<sup>[26–30]</sup> fuel cell,<sup>[31–33]</sup> and water electrolysis cells.<sup>[34]</sup> Recently, TO has gained attention for improving performance in VRFB. Yaji et al.<sup>[35]</sup> successfully implemented TO to design flow fields for VRFBs. Their 2D half-cell analysis revealed that interdigitated flow channels represent an optimal flow field configuration. The relative volume of the optimized design was found to depend on specific material properties and operating conditions, such as the prescribed porosity across the design domain and the allowable pressure drop. Notably, a higher allowable pressure drop led to an increase in the optimized porous electrode thickness, thereby enhancing the regions available for electrochemical reactions. Although the optimization parameters varied, several studies have highlighted the favorable flow characteristics of interdigititation in VRFBs.<sup>[36,37]</sup> However, flow-by architecture requires a thicker bipolar plate for machining the flow field to enhance mass transport. Therefore, some research groups are focusing on flow-through architecture by modifying PE structures using TO. Roy et al.<sup>[38]</sup> successfully designed PE architectures featuring teeth-like structures at the electrode-membrane interfaces for a non-flowing porous redox electrode system. Their topology optimization approach, which employed a binary-design method to distinguish between void and solid material regions, significantly reduced overpotentials—by 84% in redox porous electrodes and by 98% in supercapacitor electrodes. This study highlights the potential of topology optimization to enhance electrochemical performance through structural design. Additionally, Beck et al.<sup>[39]</sup> designed a porous electrode for a flow-through cell in VRFBs across various flow rates. At low flow rates, they achieved a thin and conductive geometry, while at high flow rates, they created large, low-resistance flow channels that altered both flow and conductive pathways. This optimization improved the system's power efficiency by 13.5% to 310% by distinguishing power losses into flow losses, internal electrical losses, and concentration polarization losses. Moreover, Li et al.<sup>[40]</sup> proposed a full-cell porous electrode design for a non-flow system. The penalization method was employed to obtain an optimal binary structure of the porous electrodes. Interdigitated features were observed in all optimized designs, enhancing ionic transport between the electrodes. These studies demonstrate that TO is an effective optimization approach for designing

porous electrodes, leading to improved material utilization and significantly enhanced performance.

Although recent studies have made significant advances in improving the performance of VRFBs through TO focused on reducing system losses—such as electrical and hydraulic losses—none, to our knowledge, have fully addressed the combined phenomena in both the negative and positive electrodes along with proton transport. Many existing models simplify the system to a half-cell model, incorporating only basic single-species transport, electrolyte flow, and charge transport. This approach, while useful, overlooks crucial interactions and species transport mechanisms, potentially omitting chemical species that might play critical roles in optimal electrode architecture. Consequently, designs based on these simplified models may lack the insights needed for engineering highly effective PEs. In this study, we build upon a comprehensive full-cell model developed by Tsushima and Suzuki<sup>[41]</sup> to optimize both the negative and positive electrodes within a flow-through cell design using TO. The model was modified to simulate the transient responses of VRFB cells in flow-through designs and was validated against previously published data.<sup>[42]</sup> Our objective function maximizes the overall electrochemical reaction rate while maintaining a target operating voltage of 1.2 V. To capture the variability of electrode demands under different operational conditions, we performed optimizations at three depths of discharge (DoD): 5%, 50%, 65%, 90%, and 95%. These conditions represent a spectrum from full reactant supply to near-starvation, thus allowing us to examine the specific structural requirements needed under different states of reactant availability. Each optimized electrode design, along with the unmodified electrodes in both FT (flow-through, a conventional cell architecture) and IFF (interdigitated flow field, representing a flow-by architecture), was subjected to various performance evaluations, including polarization curves and charge/discharge tests, to assess energy and round-trip efficiencies. Here, IFF specifically refers to the interdigitated flow channels machined onto the bipolar plate surface, which interface directly with the PE, as commonly used in flow-by configurations. By examining transport phenomena within the electrodes across these optimization points, we gained critical insights into how electrode structures can be fine-tuned for specific operating conditions. Our findings contribute to the body of knowledge necessary for designing PEs that maximize VRFB performance, especially as renewable energy demands continue to grow. As society moves toward carbon neutrality, these insights are essential for advancing VRFB technology to meet the requirements of a sustainable energy landscape.

## 2. Model Development

A schematic diagram showing how the VRFB works is illustrated in **Figure 1a**. An electrolyte on both the negative and positive sides is forced into the cell by pumps and circulated to the electrolyte reservoirs in each half-cell separately. Meanwhile, the circulating electrolytes, which contain active species, deliver the

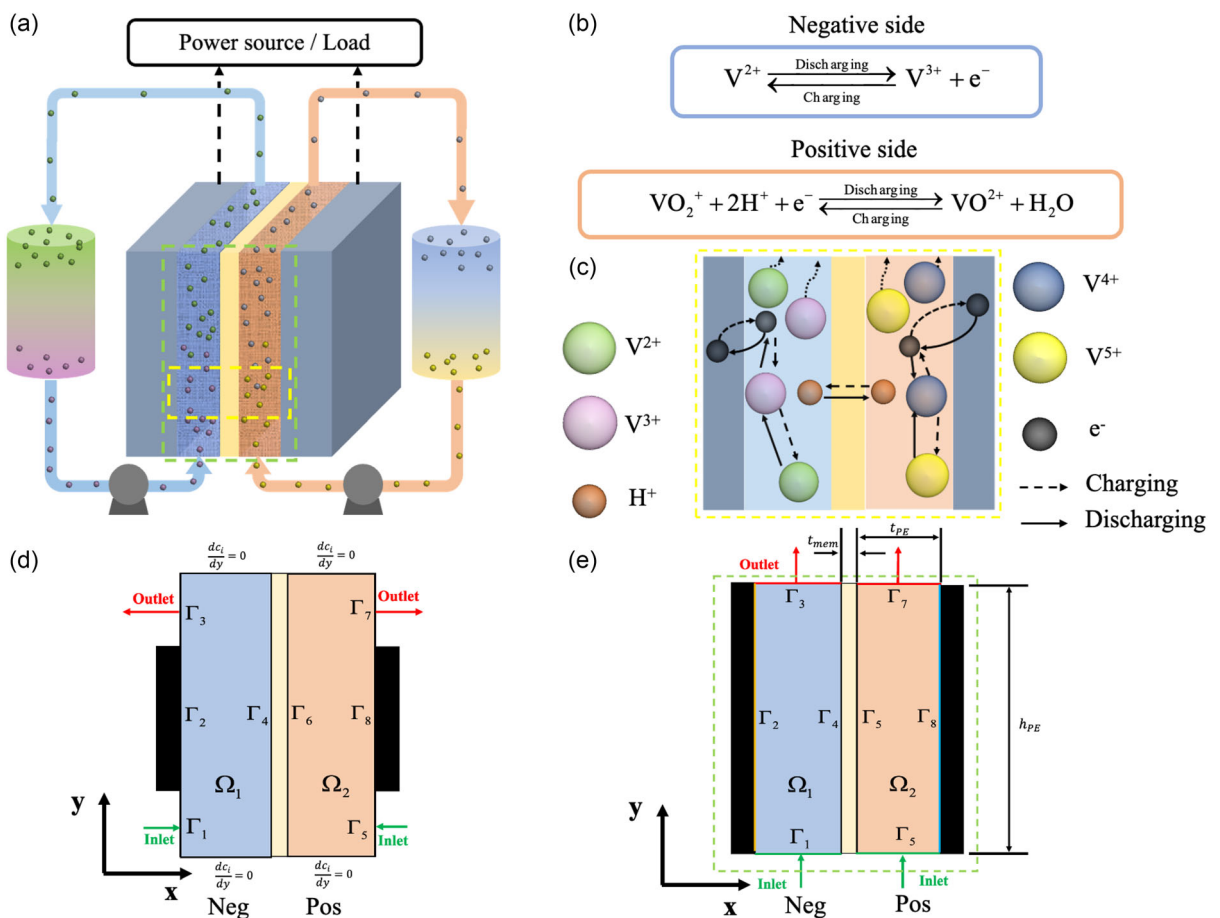


**Figure 1.** a) Schematic diagram of a VRFB operating with a flow-through cell design. b) Electrochemical reaction equations for the VRFB system. c) Schematic representation of reaction mechanisms, illustrating electron and ion transport pathways; dashed lines indicate the charging process, while solid lines represent the discharging process. d) Simplified 2D computational model of the flow-by architecture with an interdigitated flow field design, shown in the through-plane orientation. e) Simplified 2D computational model of the flow-through cell design, also shown in the through-plane orientation.

species to PE. The active vanadium species undergo electrochemical reactions to store or release electrical energy by changing their oxidation states, as illustrated in Figure 1b,c. During charging or discharging, electrons travel through the external circuit to the electrode surface, where they drive the redox reactions that change the oxidation state of the vanadium ions. Simultaneously, protons in the electrolyte migrate across the proton exchange membrane to maintain charge balance between the half-cells. This coordinated movement of electrons and protons enables the electrochemical storage and release of energy in the system.

The model geometries for the flow-by architecture, as shown in Figure 1d, were thoroughly validated in the study by Tsushima and Suzuki.<sup>[41]</sup> However, for the flow-through architecture, the model has yet to be validated. In the flow-through architecture, the modeled domain includes the negative porous electrode ( $\Omega_1$ ), the positive porous electrode ( $\Omega_2$ ), and a proton exchange membrane situated between them, as shown in Figure 1e. Electrolytes enter the system at the bottom of the domain for both the negative and positive porous electrodes, labeled as  $\Gamma_1$  and  $\Gamma_5$ , respectively. On the opposite side, the outlets for the electrolytes exiting

the negative and positive electrodes are marked as  $\Gamma_3$  and  $\Gamma_7$ , respectively. To validate the model, we compared it with experimental data from a previous study.<sup>[42]</sup> The relevant parameters used for this validation are listed in Table 1. Following the validation, optimization and further investigation were performed using parameters from Tsushima and Suzuki.<sup>[41]</sup> Table 2 summarizes the parameters employed in the optimization and investigation in this study, all of which were obtained from previous literature and the technical specifications of commercially available components.

## 2.1. Governing Equations

This study examines several physical phenomena, each governed by partial differential equations to be solved numerically. To approach this systematically, we categorize these equations into groups, presenting them along with the necessary properties for calculation. These groups include electrolyte flow and transport, active species diffusion, electrochemical kinetics, and charge transport.

**Table 1.** Parameters used for model validation.

Symbol	Unit	Description	Value	Reference
$a$	$1/m$	Active surface area	$2 \times 10^5$	[44]
$d_f$	$\mu\text{m}$	Fiber diameter	17.6	[44]
$\nu_{\text{neg}}$	$\text{Pa} \cdot \text{s}$	Kinematic viscosity of negative electrolyte	$1.07 \times 10^{-6}$	[3]
$\nu_{\text{pos}}$	$\text{Pa} \cdot \text{s}$	Kinematic viscosity of positive electrolyte	$1.07 \times 10^{-6}$	[3]
$\rho_{\text{neg}}$	$\text{kg m}^{-3}$	Density of negative electrolyte	$1.5 \times 10^3$	[3]
$\rho_{\text{pos}}$	$\text{kg m}^{-3}$	Density of positive electrolyte	$1.5 \times 10^3$	[3]
$\epsilon_0$	—	Porosity of the unmodified porous electrode	0.7	[3]
$D_{V^{2+}}$	$\text{m}^2 \text{s}^{-1}$	Diffusivity of $V^{2+}$	$2.4 \times 10^{-10}$	[45]
$D_{V^{3+}}$	$\text{m}^2 \text{s}^{-1}$	Diffusivity of $V^{3+}$	$2.4 \times 10^{-10}$	[45]
$D_{VO^{2+}}$	$\text{m}^2 \text{s}^{-1}$	Diffusivity of $VO^{2+}$	$3.9 \times 10^{-10}$	[45]
$D_{VO_2^+}$	$\text{m}^2 \text{s}^{-1}$	Diffusivity of $VO_2^+$	$3.9 \times 10^{-10}$	[45]
$D_{HSO_4^-}$	$\text{m}^2 \text{s}^{-1}$	Diffusivity of $HSO_4^-$	$1.33 \times 10^{-9}$	[44]
$k_{\text{neg}}$	$\text{m s}^{-1}$	Reaction rate constant, negative side	$1.75 \times 10^{-7}$	[46]
$k_{\text{pos}}$	$\text{m s}^{-1}$	Reaction rate constant, positive side	$3 \times 10^{-7}$	[46]
$\alpha_a$	—	Anodic transfer coefficient	0.5	[3]
$\alpha_c$	—	Cathodic transfer coefficient	0.5	[3]
$\sigma_s$	$\text{S m}^{-1}$	Electronic conductivity	$1 \times 10^3$	[3]
$\sigma_m$	$\text{S m}^{-1}$	Ionic conductivity	10	[3]
$K_{\text{CK}}$	—	Kozeny-Carman constant	5.55	[47]
$T$	K	Cell temperature	300	[3]
$i_s$	$\text{A m}^{-2}$	Current density	400	[3]
$Q_{\text{in}}$	$\text{mL s}^{-1}$	Volumetric flow rate	5	[3]
$C_{HSO_4^-}^0$	$\text{mol m}^{-3}$	Initial $HSO_4^-$ ion concentration	3000	[3]
$C_{H^+}^0$	$\text{mol m}^{-3}$	Initial $H^+$ ion concentration	3000	[3]

**Table 2.** Parameters used for optimization.

Symbol	Unit	Description	Value	Reference
$\mu_{\text{neg}}$	$\text{Pa} \cdot \text{s}$	Dynamic viscosity of negative electrolyte	$2.5 \times 10^{-3}$	[48]
$\mu_{\text{pos}}$	$\text{Pa} \cdot \text{s}$	Dynamic viscosity of positive electrolyte	$5.0 \times 10^{-3}$	[48]
$\rho_{\text{neg}}$	$\text{kg m}^{-3}$	Density of negative electrolyte	$1.3 \times 10^3$	[48]
$\rho_{\text{pos}}$	$\text{kg m}^{-3}$	Density of positive electrolyte	$1.35 \times 10^3$	[48]
$\epsilon_0$	—	Porosity of the unmodified porous electrode	0.83	[41]
$D_{V^{2+}}$	$\text{m}^2 \text{s}^{-1}$	Diffusivity of $V^{2+}$	$2.4 \times 10^{-10}$	[48]
$D_{V^{3+}}$	$\text{m}^2 \text{s}^{-1}$	Diffusivity of $V^{3+}$	$2.4 \times 10^{-10}$	[48]
$D_{VO^{2+}}$	$\text{m}^2 \text{s}^{-1}$	Diffusivity of $VO^{2+}$	$3.9 \times 10^{-10}$	[48]
$D_{VO_2^+}$	$\text{m}^2 \text{s}^{-1}$	Diffusivity of $VO_2^+$	$3.9 \times 10^{-10}$	[48]
$D_{H^+}$	$\text{m}^2 \text{s}^{-1}$	Diffusivity of $H^+$	$9.3 \times 10^{-9}$	[46]
$D_{HSO_4^-}$	$\text{m}^2 \text{s}^{-1}$	Diffusivity of $HSO_4^-$	$1.33 \times 10^{-9}$	[48]
$D_{SO_4^{2-}}$	$\text{m}^2 \text{s}^{-1}$	Diffusivity of $SO_4^{2-}$	$1.06 \times 10^{-9}$	[48]
$k_{\text{neg}}$	$\text{m s}^{-1}$	Reaction rate constant, negative side	$2.21 \times 10^{-7}$	[41]
$k_{\text{pos}}$	$\text{m s}^{-1}$	Reaction rate constant, positive side	$8.84 \times 10^{-7}$	[41]
$\alpha_a$	—	Anodic transfer coefficient	0.5	[41]
$\alpha_c$	—	Cathodic transfer coefficient	0.5	[41]
$\beta$	—	$HSO_4^-$ degree of dissociation	0.25	[48]
$\sigma_s$	$\text{S/m}$	Electronic conductivity	$6.05 \times 10^2$	[48]
$\sigma_m$	$\text{S/m}$	Ionic conductivity	2.95	[41]

### 2.1.1. Electrolyte Transport

Electrolytes are assumed to be incompressible fluids, governed by the continuity and Navier–Stokes equations as shown in the following:

$$\nabla \cdot \vec{u} = 0 \quad (1)$$

$$-\nabla p + \mu \nabla \cdot \vec{u} - \alpha \vec{u} = 0 \quad (2)$$

where  $\vec{u}$ ,  $p$ ,  $\mu$ , and  $\alpha$  are the velocity, the pressure, the dynamic viscosity, and the inverse permeability.

To model electrolyte flow within porous media, Darcy's drag term is incorporated, simplifying the complex structure into a homogeneous model, as represented by the inverse permeability expressions in Equation (3)

$$\alpha = \frac{\mu}{k_f} \quad (3)$$

where  $k_f$  is the permeability ( $\text{m}^2$ ), which is described by Kozeny–Carman equation as shown below in Equation (4)

$$k_f = \frac{d_f^2 \epsilon^3}{16 K_{\text{KC}} (1 - \epsilon)^2} \quad (4)$$

where  $d_f$ ,  $\epsilon$ , and  $K_{\text{KC}}$  are the average fiber diameter, the local porosity, and the Kozeny–Carman constant.

### 2.1.2. Mass Transportation

In simulating a VRFB system, it is essential to include the concentration distributions of specific species, namely  $V^{2+}$ ,  $V^{3+}$ ,  $V^{4+}$ ,  $V^{5+}$ ,  $H^+$ , and  $\text{HSO}_4^-$ , using the mass balance within the porous electrode domain, governed by the Nernst–Planck equation.

$$\nabla \cdot \vec{N}_i = -R_i \quad (5)$$

$$\vec{N}_i = -D_i^{\text{eff}} \nabla c_i - z_i u_{\text{mobi}} F c_i \nabla \varphi_i + c_i \vec{u} \quad (6)$$

where  $\vec{N}_i$ ,  $R_i$ ,  $z_i$ ,  $u_{\text{mobi}}$ ,  $c_i$ , and  $F$  are the species flux, the source term of active species, the charge number, the ionic mobility in the electrolyte, the bulk concentration, and the Faraday constant. Source terms of each chemical species are summarized in Table 3.

In the computational domain, considered as a porous electrode, the solid-phase fractions are incorporated into physical parameters like diffusivity and electronic conductivity, using the Bruggeman correlation as shown below:

$$D_i^{\text{eff}} = \epsilon^{3/2} D_i \quad (7)$$

$$\sigma_s^{\text{eff}} = (1 - \epsilon)^{3/2} \sigma_s \quad (8)$$

where  $D_i$ ,  $\epsilon$ , and  $\sigma_s$  are the diffusivity of each species, the porosity, and the electronic conductivity. Ionic mobility within the porous electrode through the electrolyte is calculated using the Nernst–Einstein equation. This approach enables us to quantify the relationship between ion diffusion and electric field effects, key

**Table 3.** Source terms of each chemical species.

Species	Calculated domains	Source term
$V^{2+}$	Negative PE	$j_{\text{neg}}/F$
$V^{3+}$	Negative PE	$-j_{\text{neg}}/F$
$V^{4+}$	Positive PE	$j_{\text{pos}}/F$
$V^{5+}$	Positive PE	$-j_{\text{pos}}/F$
$H^+$	Negative PE	$-R_d$
$H^+$	Positive PE	$-2j_{\text{neg}}/F - R_d$
$\text{HSO}_4^-$	Negative PE	$R_d$
$\text{HSO}_4^-$	Positive PE	$R_d$

factors that influence ion transport efficiency within the complex porous structure of the electrode.

$$u_{\text{mobi}} = D_i^{\text{eff}}/RT \quad (9)$$

where  $R$  is the universal gas constant and  $T$  is the temperature.

To determine surface concentration, the local mass transfer coefficient ( $k_m$ ) is essential. This coefficient was obtained through an empirical correlation dependent on the local velocity within the porous regions. Relevant dimensionless numbers are incorporated as shown below:

$$Sh = aRe^bSc^c = k_{m,a} d_{f,a}/D_a \quad (10)$$

where  $a$ ,  $b$ , and  $c$  are the fitting parameters, equal to 0.38, 0.78, and 0.3,<sup>[41]</sup> respectively.  $Re$ ,  $Sc$ ,  $k_{m,a}$ ,  $d_{f,a}$ , and  $D_a$  are the Reynolds number, the Schmidt number, the mass transfer coefficient, the particle diameter, and the bulk diffusivity of vanadium species. The subscript  $a$  indicates whether the negative or positive side is being considered.

The species concentrations at the solid–liquid interfaces within porous regions are related to the bulk concentration, determined by the balance between the mass transfer flux of vanadium ions in the bulk electrolyte and the reaction flux at the electrode surface. An example for calculating  $c_{\text{VO}^{2+}}^s$  and  $c_{\text{VO}_2^+}^s$  is provided as follows

$$N_{\text{VO}^{2+}}^s = k_{m,\text{pos}} (c_{\text{VO}^{2+}} - c_{\text{VO}^{2+}}^s) = i_{\text{pos}}/aF \quad (11)$$

$$N_{\text{VO}_2^+}^s = k_{m,\text{pos}} (c_{\text{VO}_2^+} - c_{\text{VO}_2^+}^s) = -i_{\text{pos}}/aF \quad (12)$$

where  $i_{\text{pos}}$  is the current density in positive electrode and  $a$  represents the local active surface area across the calculated domains.

### 2.1.3. Charge Transport

To simulate the charge transport phenomena in the solid phase, Ohm's law was employed, as expressed in Equation (13). Additionally, the ion transport in the liquid phase was determined by the Faraday's law in Equation (14).

$$\nabla \cdot i_s = \sigma_s^{\text{eff}} \nabla \varphi_s = -j \quad (13)$$

$$\nabla \cdot i_i = F \sum_i z_i \vec{N}_i = j \quad (14)$$

When modeling the VRFB as a full cell system, it is essential to account for the proton transport mechanisms due to their critical role in facilitating the electrochemical reactions. During the discharging process of the VRFB, protons move across the membrane from the negative electrode to the positive electrode. Conversely, during charging, protons migrate in the opposite direction. The ionic conductivity of the membrane, as described in Equation (15), governs this proton transfer.

$$\nabla \cdot i_l = \sigma_l \nabla \varphi_l = 0 \quad (15)$$

where  $\sigma_l$  is the ionic conductivity.

#### 2.1.4. Electrochemical Kinetics

Electrochemical kinetics were modeled using the Butler–Volmer equation, which relies on the surface concentration of species to determine the local current density for both the negative and positive electrodes.

$$j_{\text{neg}} = Fk_{\text{neg}} C_{V^{2+}}^{\alpha_c} C_{V^{5+}}^{\alpha_a} \left[ \frac{C_{V^{2+}}}{C_{V^{5+}}} \exp\left(\frac{-\alpha_c F\eta}{RT}\right) - \frac{C_{V^{5+}}}{C_{V^{2+}}} \exp\left(\frac{\alpha_a F\eta}{RT}\right) \right] \quad (16)$$

$$j_{\text{pos}} = Fk_{\text{pos}} C_{V^{4+}}^{\alpha_c} C_{V^{3+}}^{\alpha_a} \left[ \frac{C_{V^{4+}}}{C_{V^{3+}}} \exp\left(\frac{-\alpha_c F\eta}{RT}\right) - \frac{C_{V^{3+}}}{C_{V^{4+}}} \exp\left(\frac{\alpha_a F\eta}{RT}\right) \right] \quad (17)$$

where  $k$ ,  $\alpha$ ,  $\eta$  are the reaction rate, the charge transfer coefficient, and the overpotential, respectively. The subscripts neg and pos denote the operating sides, specifically the negative and positive poles, respectively. Additionally, a and c represent anodic and cathodic processes, respectively.

Furthermore, to solve the Butler–Volmer equation, the overpotentials must be determined, which are calculated using Equation (18) and (19).

$$\eta_{\text{neg}} = \varphi_s - \varphi_l - E_{\text{eq,neg}} \quad (18)$$

$$\eta_{\text{pos}} = \varphi_s - \varphi_l - E_{\text{eq,pos}} \quad (19)$$

where  $\varphi_s$  is the electric potential,  $\varphi_l$  is the electrolyte potential, and  $E_{\text{eq}}$  is the open circuit potential.

To determine the open circuit potential, the Nernst equation was used for the calculations.

$$E_{\text{eq,neg}} = E_{0,\text{neg}} - \frac{RT}{F} \ln\left(\frac{C_{V^{5+}}}{C_{V^{2+}}}\right) \quad (20)$$

$$E_{\text{eq,pos}} = E_{0,\text{pos}} - \frac{RT}{F} \ln\left(\frac{C_{VO_2^+} C_{H^+}^2}{C_{VO^{2+}}}\right) \quad (21)$$

where  $E_{0,\text{neg}}$  is the equilibrium potential of the negative side and  $E_{0,\text{pos}}$  is the equilibrium potential of the positive side.

In the acidic solution containing vanadium species, specifically aqueous sulfuric acid, protons are produced at both the negative and positive electrodes through a two-step dissociation process, as illustrated in the following



A two-step dissociation is assumed to occur simultaneously as a spontaneous reaction. The rate of production is determined using  $R_d$ , as described by the following equation:

$$R_d = -k_d \left( \frac{c_{H^+} - c_{HSO_4^-}}{c_{H^+} + c_{HSO_4^-}} - \beta \right) \quad (24)$$

where  $k_d$  is the dissociation rate and  $\beta$  is the degree of dissociation of  $HSO_4^-$ .

#### 2.2. Transient Response Modeling

This study examines both the IV polarization curve, allowing for the evaluation of losses at specific load or supply conditions, as well as the charge and discharge capacity of the system. Typically, IV polarization curve simulations assume a steady-state system, allowing the equations to be solved without considering transient responses. However, to examine how electrode structure impacts charging and discharging capacity, a model that captures changes in active species concentration over time is required. This enables simulation of charge and discharge curves as active species are gradually consumed. To address this, we developed a simple model that varies the boundary conditions at the inlets over time, providing insight into the dynamic behavior of the system. Accordingly, the rate of mass change in the electrolyte tank is set to match the reaction rate within the cell. For example, during the discharge process on the negative side, the rate of change for vanadium species involves the consumption of  $V^{2+}$  as it converts to  $V^{3+}$  through the electrochemical reaction. Consequently, the inlet concentration of  $V^{2+}$  decreases over time as it is consumed.

$$\left[ \frac{dc}{dt} \right]_{\text{tank}} = \frac{A_{\text{ele}}}{V_{\text{tank}}} \frac{[i]_{\text{cell}}}{F} \quad (25)$$

where  $A_{\text{ele}}$  is active area of VRFB cell,  $V_{\text{tank}}$  is volume of electrolyte in the tank, and  $i$  is current density

#### 2.3. Topology Optimization

This study utilizes TO to determine the optimal structure for each porous electrode on both sides at three different DoDs within a flow-through architecture. These optimized structures will be compared with unmodified electrode structures in both flow-through and flow-by architectures (with IFFs), where the porosity of the unmodified electrodes corresponds to that of commercially available electrodes. Here, the design domains are defined as the porous electrodes on both sides, using porosity as the design variable within a density-based method. The optimization conditions were established by defining the operating voltage, simplifying the design process for the VRFB stack. The search for the optimized structure focuses on maximizing the reaction rates of both the negative and positive electrodes. Consequently, the objective function, along with its constraints, can be formulated as follows

$$\begin{aligned} \text{Maximize}_{\varepsilon_1(x), \varepsilon_2(x)} \quad & F = \int \left| \frac{j_{R,\text{neg}}}{F} \right| d\Omega_1 + \int \left| \frac{j_{R,\text{pos}}}{F} \right| d\Omega_2 \\ \text{Subject to} \quad & \mathbf{G}_0 = 0, \end{aligned} \quad (26)$$

$$0 < \varepsilon_1(x) < 1 \text{ and } 0 < \varepsilon_2(x) < 1 \text{ for } \forall x \in \Omega_i$$

Here,  $\varepsilon_{\text{neg}}$  and  $\varepsilon_{\text{pos}}$  represent the design variables in the density-based topology optimization model, corresponding to the negative and positive PE domains, respectively. Although the model couples the entire electrochemical system, the optimization is applied to each electrode domain independently.

Gradient-based TO was performed in COMSOL Multiphysics utilizing the adjoint state method, with the adjoint equation expressed in a general form as follows

$$\left( \frac{\partial \mathbf{G}_0}{\partial \mathbf{U}} \right)^T \lambda = - \left( \frac{\partial F_{\text{obj}}}{\partial \mathbf{U}} \right)^T \quad (27)$$

where  $\lambda$  is the vector of adjoint variable,  $\mathbf{G}_0$  is the set of governing partial differential equations,  $\mathbf{U}$  is vector of state variable, and  $F_{\text{obj}}$  is the set objective functions involving in the systems. The adjoint equation was solved to determine the adjoint variable, which was then used in the sensitivity analysis. The general form is expressed as follows

$$\frac{\partial F_{\text{obj}}}{\partial \psi_i} = \frac{\partial F_{\text{obj}}}{\partial \psi_i} + \lambda^T \frac{\partial \mathbf{G}_0}{\partial \psi_i} \quad (28)$$

In the optimization process, sensitivity is calculated and applied to update the design variables. Filtering is essential to ensure smoothness, preventing the formation of checkerboard patterns—artificial oscillations in design variables across the fixed domain that can lead to impractical or uneven material distributions. Additionally, filtering helps maintain the smoothness of the design variables, ensuring a more realistic and manufacturable structure.

To achieve this, the design variables were modified using a Helmholtz-type filter,<sup>[43]</sup> represented by the partial differential equation shown below. The Helmholtz filter serves to regulate spatial variations in design variables, creating a smoother and more continuous topology throughout the optimization process.

$$\theta_f = R^2 \nabla^2 \theta_f + \theta_c \quad (29)$$

where  $\theta_c$ ,  $\theta_f$ ,  $R$  are the design variable, the filtered design variable, and the filter radius, respectively. Throughout the optimization process, design variables range from 0 to 1, representing fully electrode material (0) and fully flow channel (1), respectively. To compute the associated material properties at intermediate porosity values, we implemented a convex interpolation function for the mass transfer coefficient  $k_m$ , inverse permeability  $\alpha$ , and specific surface area ( $a$ ), following the formulation approach used in Yaji et al.<sup>[35]</sup> Unlike binary-design approaches, our use of interpolation is intended to support continuous spatial variation of porosity and to improve numerical convergence throughout the optimization process.

In particular, interpolation of the specific surface area was included because it directly governs the amount of electrochemically active surface available for redox reactions. This enables the

optimizer to balance material distribution with local reaction demands, resulting in functionally graded structures that adapt to varying transport and kinetic limitations across the PE domain.

$$k_e = \frac{q(1 - \varepsilon_i)}{q + \varepsilon_i} k_m \quad (30)$$

$$\alpha_e = \frac{q(1 - \varepsilon_i)}{q + \varepsilon_i} \alpha \quad (31)$$

$$a_e = \frac{q(1 - \varepsilon_i)}{q + \varepsilon_i} a \quad (32)$$

where  $q$  is the convexity controlling parameter and  $\varepsilon_i$  is the density function, which is replaced by  $\varepsilon_{\text{neg}}$  or  $\varepsilon_{\text{pos}}$  depending on the operating side of PE. The lower bound of design variables was set to 0.1 to prevent fully material-filled regions where no-slip conditions would be applied, which could otherwise lead to computational instability, and the move limit was set as  $5 \times 10^{-2}$ .

To enhance clarity regarding the key variables involved in the optimization framework, we provide the following brief overview: 1) The mass transfer coefficient ( $k_m$ ) governs the rate of species transport from bulk electrolyte to the reactive surface. 2) The inverse permeability ( $\alpha$ ) represents fluid resistance through the porous medium, affecting electrolyte flow. This term is modeled following Equation (3), which reflects the structure-dependent nature of permeability in fibrous porous electrodes. 3) The specific surface area ( $a$ ) determines the amount of active area available for electrochemical reactions. This variable is especially critical in conductivity-retaining porous media, where maintaining both surface area and electron pathways is necessary for efficient operation.

Each of these parameters is interpolated within the topology optimization framework as a function of local porosity (design variable), enabling the optimizer to modify electrode structure based on transport and reaction requirements. This formulation ensures that the model accurately reflects the complex interplay between flow behavior, species transport, and electrochemical performance within the porous electrode domains.

In electrochemical energy devices, two primary optimization approaches are typically applied. The first approach fixes the current density while minimizing the overpotential, thus maximizing the cell voltage. The second approach fixes the cell voltage and searches for an optimal configuration to maximize current density. Recently, a new study introduced an optimization method to achieve maximum power output by not restricting the boundary conditions.<sup>[29]</sup> However, for the purposes of this study, optimization was conducted under a fixed cell voltage, chosen at 1.2 V, which supports stack designers in developing effective stack configurations by maximizing current density. At the inlet, the pressure driving the electrolyte was set to  $2 \times 10^5 + P_{\text{out}}$  Pa to ensure a fair comparison between the optimization cases. To accommodate varying DoDs, five DoDs were considered in the optimization process, achieved by adjusting inlet concentrations. A summary of the conditions used in this optimization is provided in **Table 4**.

Table 4. Boundary conditions used in the optimization processes.			
Parameter	Unit	Description	Value
$P_{in}$	Pa	Pressure prescribes	$2 \times 10^5 + P_{out}$
$P_{out}$	Pa	Outlet pressure	$1.01325 \times 10^5$
$\phi_s$	V	Electrode potential	1.2
$c_{ini}$	mol m <sup>-3</sup>	Initial reactant concentration at specified DoDs	1520, 1440, 1040, 800, 80
$q$	–	Convex interpolation parameter	0.01
$h$	–	Move limit	0.05

Table 5. Boundary conditions for simulating the polarization and charge-discharge curves.			
Parameters	Unit	Description	Value
$Q_{in}$	mL min <sup>-1</sup>	Electrolyte flow rate	1, 3, 5
$i$	A cm <sup>-2</sup>	Current density	0 – 2.5
$P_{out}$	Pa	Outlet pressure	$1.01325 \times 10^5$
$T$	K	Cell temperature	298

After optimizing the porous electrodes, five optimized electrode structures were evaluated for IV performance under conditions of a  $3 \text{ mL min}^{-1}$  electrolyte flow rate (for a  $5 \text{ cm}^2$  cell) and an electrolyte DoD of 5%. A transient response model was then used to simulate the charge/discharge curves, keeping the flow rate steady at  $3 \text{ mL min}^{-1}$  with a charge/discharge current density of  $100 \text{ mA cm}^{-2}$ . The electrolyte tank was set at 30 mL with an initial DoD of 5%. To assess the efficiency of these optimized structures relative to the unmodified electrode structure, the electrolyte flow rate was varied from 1 to  $5 \text{ mL min}^{-1}$ , allowing for a performance comparison across flow rates. Table 5 summarizes the conditions used for the investigation in this study.

#### 2.4. Performance Evaluation Matrices

Following the charge/discharge simulation, several performance evaluation metrics can be used to assess the performance of different electrode structures, including energy efficiency, hydraulic power loss, round-trip efficiency, and electrolyte utilization. The energy efficiency (EE) is defined as shown in Equation (33).

$$\text{EE} = \frac{\int_0^{t_{\text{Dchg}}} V_{\text{cell}}(t) I_{\text{Dchg}} dt}{\int_0^{t_{\text{Chg}}} V_{\text{cell}}(t) I_{\text{Chg}} dt} \quad (33)$$

where  $V_{\text{cell}}$ ,  $I$ ,  $t$  represent the measured cell voltage, current, and time, respectively. Note that the subscripts *dischg* and *chg* denote discharging and charging conditions, respectively. Hydraulic power loss ( $P_{\text{loss}}$ ) refers to the power required to drive the electrolyte through the VRFB cell and is calculated using Equation (34). Accordingly, the hydraulic energy loss (HEL) can be determined as the minimum energy required to operate the circulation pump during charging and discharging, which depends on the structure

of the PEs as well as the charging and discharging times, as given by Equation (35).

$$P_{\text{loss}} = \frac{\Delta p_{\text{neg}} Q_{\text{in}}}{\eta_{\text{pump}}} + \frac{\Delta p_{\text{pos}} Q_{\text{in}}}{\eta_{\text{pump}}} \quad (34)$$

$$\text{HEL} = (P_{\text{loss}} \times t_{\text{Dchg}}) + (P_{\text{loss}} \times t_{\text{Chg}}) \quad (35)$$

Here,  $\Delta p$  represents the pressure drop across the porous electrode domain, and  $\eta_{\text{pump}}$  denotes the pump efficiency.

The round-trip efficiency (RTE) represents the overall efficiency of the system. In redox flow batteries, unlike lithium-ion or other conventional batteries that operate without auxiliary systems, external pumping is required to circulate the electrolytes through the cell. This introduces an additional energy demand associated with electrolyte circulation. As described in Equation (35), the HEL quantifies the energy required to overcome flow resistance within the system, which depends on both the cell architecture and the distribution of material density in the PEs. To accurately assess the overall system performance, is considered by incorporating the energy consumed by the pump during both charging and discharging cycles, as defined in Equation (36).

$$\text{RTE} = \frac{\int_0^{t_{\text{Dchg}}} V_{\text{cell}}(t) I_{\text{Dchg}} dt - P_{\text{loss}} t_{\text{Dchg}}}{\int_0^{t_{\text{Chg}}} V_{\text{cell}}(t) I_{\text{Chg}} dt + P_{\text{loss}} t_{\text{Chg}}} \quad (36)$$

The electrolyte utilization (EU) provides a quantitative measure of how effectively the electrolyte is used within the cell, which is defined mathematically in Equation (37).

$$\text{EU} = \frac{\text{Discharge capacity}}{\text{Theoretical capacity}} \quad (37)$$

## 3. Results and Discussion

Our model was validated using a system with an electrode measuring  $100 \times 100 \text{ mm}$  in width and height, with a thickness of 3 mm, while the membrane had a thickness of 180 microns.<sup>[42]</sup> The model validation was performed to confirm that the geometries are suitable for a flow-through cell design and that the transient response model reliably captures system behavior, despite being implemented in a 2D framework. The results, shown in Figure 2, indicate that the model successfully replicates the experimental data with a reasonable degree of accuracy. The average absolute error over the entire charge and discharge cycles is calculated to be 2.795%, which is considered acceptable for validating the numerical model. This level of error suggests that the underlying physical assumptions and governing equations used in the simulation are sufficiently robust for capturing the key electrochemical and transport phenomena within the system. Minor discrepancies may be attributed to experimental uncertainties, simplifications in geometry, or assumptions such as constant material properties and ideal flow behavior. Consequently, the model is deemed adequate for further optimization and investigation.

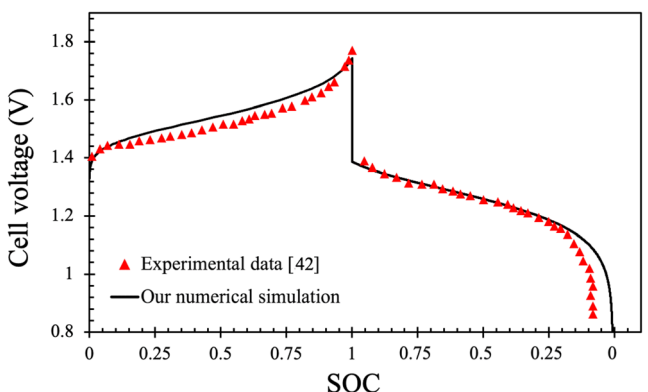


Figure 2. Comparison of simulation results with experimental data.<sup>[42]</sup>

This study aimed to design optimal PE structures for VRFBs through TO by maximizing reaction rates for both the negative and positive PEs within a full cell model, moving beyond intuition-based designs. The resulting PE structures were evaluated across key performance metrics under varying operating conditions to provide insights into transport behaviors within the cell, thereby enhancing understanding of how PE modifications can improve VRFB performance. The convergence history of the objective function, illustrated in Figure 3a–e, demonstrates significant improvements in reaction rate at 5%, 50%, 65%, 90%, and 95% DoD, with all optimizations converging effectively. By overlaying PE structures in the convergence plot, the evolution of PEs during calculation is visualized, showing the positive electrode on the right and the negative on the left. The results reveal interdigitated-like structures in both the negative and positive electrodes. For OFT5%, OFT50%, OFT65%, and OFT90%, the negative electrode structures exhibit a similar trend, consisting only of main branches. However, at OFT95%, the negative electrode displays a distinct interdigitated-like structure, with smaller secondary branches emerging from the main branches. The average porosity of these structures across the entire negative electrode domain is  $\approx 0.45\text{--}0.50$ .

On the positive PE, the interdigitated-like structures at OFT5% and OFT50% exhibit a greater number of high-porosity branches compared to the negative side. At OFT65% and OFT90%, high-porosity channels are formed predominantly at the membrane/electrode and current collector/electrode interfaces. At OFT95%, again, smaller branches emerge from these high-porosity channels. Overall, unlike the negative electrode, the average porosity of the optimized structures on the positive side is  $\approx 0.37\text{--}0.43$ . Figure 3f reveals the final optimized structures at different DoDs, with interdigitated-like channels emerging in the on both negative and positive PEs. The formulation of smaller branches from the high porosity channels in OFT95% indicates adaptive structural changes in response to reactant availability.

To analyze how material distribution enhances the cell's current density, the porosity was averaged and plotted along the x-axis to obtain the 1D projected porosity profiles of the negative and positive electrodes across each case. The projected porosity along x-axis (representing the normalized distance from the

membrane/electrode interface) is shown in Figure 4a,b. For the negative electrode, the projected porosity along the x-axis of all optimized structures shows a consistent pattern, with a pronounced decrease at the middle of the PE as well as at the membrane/electrode and current collector/electrode interfaces. The porosity ranges from  $\approx 0.3$  to  $0.7$ , with OFT95% exhibiting a slightly higher value. For the positive electrode, the x-axis projection reveals a different distribution. While most cases show only minor differences, OFT65% and OFT90% display larger porosity near the interfaces and relatively lower porosity in the middle of the PE. In contrast, OFT95% exhibits an overall higher porosity compared to the others.

The projected porosity along the y-axis, representing the normalized distance from inlet to outlet, is illustrated in Figure 4c,d. In the negative electrode, the porosity exhibits a consistent pattern of  $\approx 0.4\text{--}0.5$  for OFT5%, OFT50%, OFT65, and OFT 90%. Additionally, at 95% DoD, the average porosity decreases approximately from 0.48 to 0.6. This increase which was also found in positive PEs occurs because the optimization condition at 95% DoD represents a scenario where the reactant for the electrochemical reaction is nearly depleted. To enhance reactivity under these conditions, mass transport is promoted in both the negative and positive PE domains through the formation of higher-porosity regions and smaller branches. These features facilitate reactant movement and increase the transport of active species, thereby improving electrochemical performance. Overall, the OFT95% design incorporate increased porosity across the PE domains—particularly along the y-axis projection—to meet the heightened reaction demands driven by mass transport limitations under low reactant concentration conditions.

The porosity distributions shown in Figure 4 further highlight the adaptive behavior of the topology optimization across different DoD. In the OFT5%, OFT50%, OFT65%, and OFT90% designs, the negative electrode forms flow branches only at the membrane and current collector interfaces, without any smaller branches emerging from the main branch. This suggests that under conditions where reactant concentration is not severely depleted, the system favors creating active surface areas for reactivity with simple reactant supply channels within the PEs, rather than complex structural designs, since mass transport limitations have not yet become dominant.

In contrast, the positive electrode exhibits more complex structural development. This outcome is closely associated with the proton requirements of the positive half-cell reaction. Even when vanadium availability is sufficient, limited proton accessibility can become a performance bottleneck—especially under forced flow-through conditions. As a result, the design incorporates high-porosity regions to guide electrolyte flow and enhance proton distribution, while retaining denser regions to preserve electrochemically active surface area and improve electron mobility during the electrochemical process. The OFT95% case displays a different structure in both electrodes. At this high DoD, the system operates under reactant-starved conditions, making mass transport the dominant performance constraint. In response, topology optimization introduces more branched designs and higher porosity in both the positive and negative

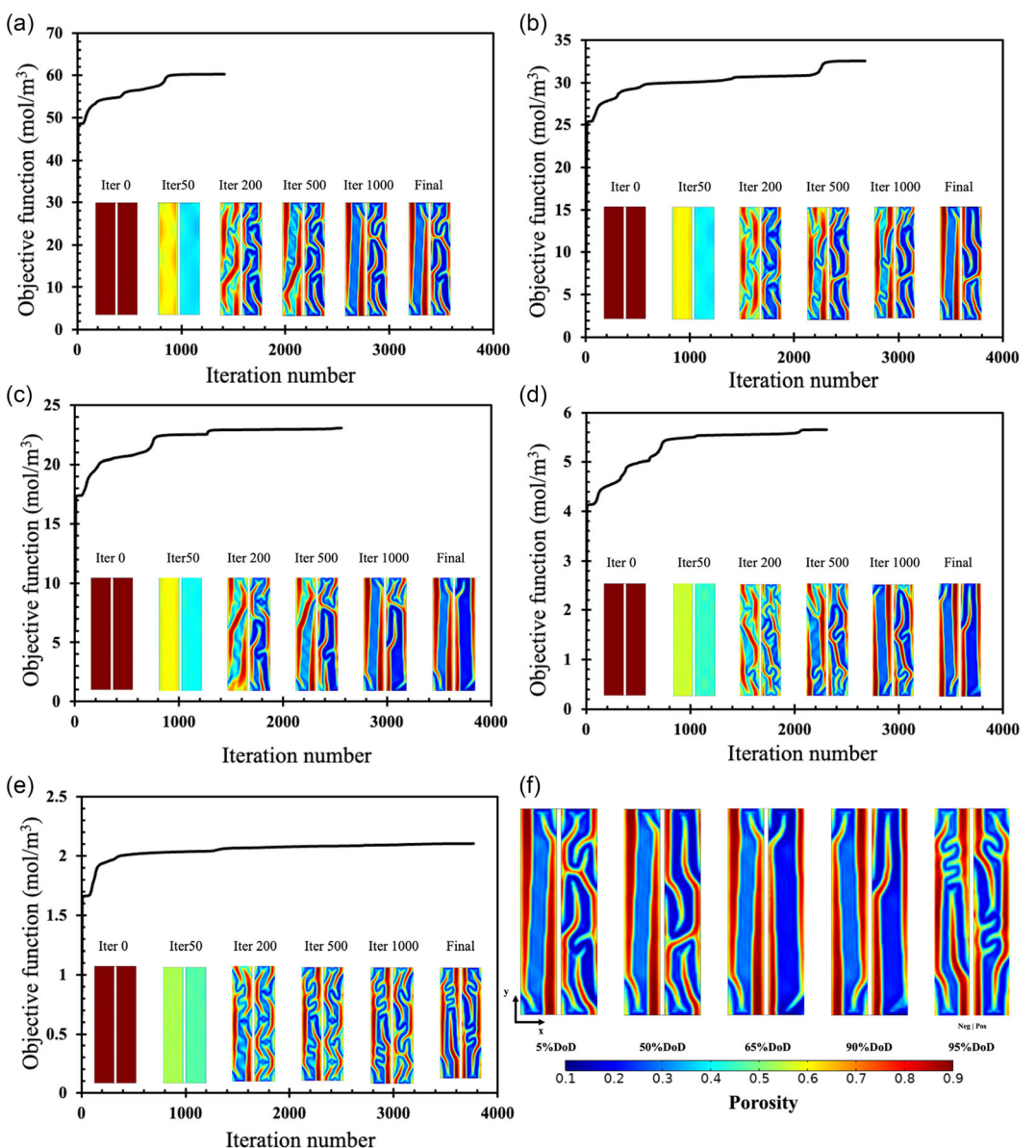


**Figure 3.** Convergence history of the objective function for the OFT electrode at a) 5% DoD, b) 50% DoD, c) 65% DoD, d) 90% DoD, and e) 95% DoD. f) The resulting heterogeneous structures from the optimization process, showing variations in porosity for OFT at 5%, 50%, 65%, 90%, and 95% DoD.

electrodes. These features promote deeper penetration of the electrolyte into active regions and help maintain performance despite low species concentrations. The resulting architectures reflect a careful tradeoff between transport facilitation and surface material preservation, especially under the prescribed pressure boundary condition, which penalizes designs with high flow resistance. This progression across DoD levels demonstrates the effectiveness of the porosity-based optimization approach in adapting to electrochemical and transport demands under different operating conditions.

The polarization curve is used to evaluate the performance of optimized PEs at five different DoDs using the OFT design. These are compared against unmodified electrode structures operating in both FT and IFF cell architectures. In this comparison, the

electrolyte flow rate was set at 1, 3, and 5 mL min<sup>-1</sup>, while the current density was varied from 0 to 1.7–2.5 A cm<sup>-2</sup> at a DoD of 5%. This setup ensures a sufficient supply of active species for electrochemical reactions at the reactive surfaces, as illustrated in Figure 5.

The IV polarization curves in Figure 5 show that unmodified electrodes (both FT and IFF designs), characterized by a homogeneous structure, begin to diverge from the OFT at low current densities due to increased losses. As current density rises, the polarization curves for the FT and IFF designs exhibit minimal differences. However, within the current density range of ≈0.1, 0.4, and 0.6 A cm<sup>-2</sup>, the FT cell design reaches a limiting current at flow rates of 1, 3, and 5 mL min<sup>-1</sup>, respectively, whereas the IFF design demonstrates a higher limiting current of about

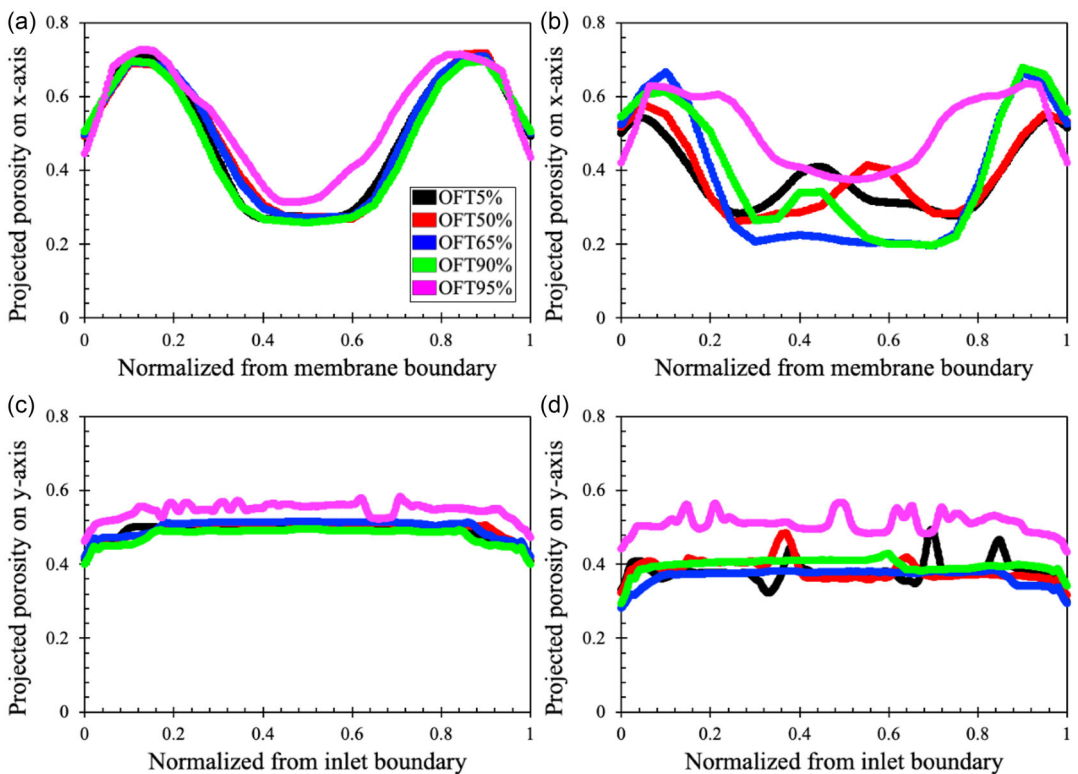


**Figure 4.** Projected porosity values for optimized porous electrodes at 5%, 50%, 65%, 90%, and 95% DoD: a) along the x-axis for the negative PE, b) along the x-axis for the positive PE, c) along the y-axis for the negative PE, and d) along the y-axis for the positive PE.

0.25, 0.75, and  $1.1 \text{ A cm}^{-2}$  at flow rates of 1, 3, and  $5 \text{ mL min}^{-1}$ , respectively. The advantage of the IFF design lies in its flow characteristics; the electrolyte's flow paths under the rib region enhance convective forces, facilitating the concentration of active species. Consequently, the absence of mass transport limitations at the same operating current density range results in an increased power density, rising from  $0.168$ ,  $0.424$ , and  $0.622 \text{ W cm}^{-2}$  for the FT design to  $0.286$ ,  $0.627$ , and  $0.827 \text{ W cm}^{-2}$  for the IFF design at flow rates of 1, 3, and  $5 \text{ mL min}^{-1}$ , respectively. The OFTs outperformed the homogeneous structures across all regions, with all five OFTs demonstrating similar performance at low and intermediate current densities. For instance, when operating at  $3 \text{ mL min}^{-1}$ , in scenarios where the electrode structure was optimized for 5%, 50%, 65%, and 90%DoD, the limiting currents were comparable, hovering around  $1.2 \text{ A cm}^{-2}$ . In contrast, the limiting current for the electrode optimized at 95%DoD exceeded  $1.4 \text{ A cm}^{-2}$ . Notably, while the unmodified PE in the FT configuration performed significantly worse than the unmodified PE in the IFF, optimizing the electrode structure in the FT setup can lead to a substantial performance boost, allowing it to even surpass the performance of the IFF. This is significant, as the IFF represents one of several flow-by cell designs that significantly improve mass transport, promoting a uniform distribution of electrolyte between the inlet and outlet manifolds.<sup>[16,42]</sup>

Figure 6 illustrates the charge and discharge characteristics of various porous electrodes in comparison to the IFF, at various electrolyte flow rates and charging/discharging current densities.

Consistent with the IV performance curve shown in Figure 5, the cell voltage during discharge for both the FT and IFF was lower, while during charging, it was higher compared to the OFTs. The FT design exhibited a lower capacity than the IFF due to its inferior handling of mass transport losses. Among all configurations evaluated, the OFT 90% and OFT95%, optimized for relatively low reactant concentration, demonstrated the best performance in terms of charge/discharge capacity at lower flow rates and higher current densities (bottom left regions of Figure 6). We further examined electrolyte utilization at varying flow rates and current densities to understand how each configuration impacts overall efficiency. Higher EU corresponds to greater energy density for the VRFB system, as less surplus electrolyte is required, which ultimately reduces electrolyte costs. The results show that the OFT90% and OFT95% configurations deliver slightly higher performance than the others across all flow rates and current densities, particularly when compared with the unmodified PE in the FT and IFF configurations. For example, at a volumetric electrolyte flow rate of  $3 \text{ mL min}^{-1}$  and a current density of  $100 \text{ mA cm}^{-2}$ , these configurations achieved a notably high EU of  $\approx 80\%$ . Even at a higher current density of  $150 \text{ mA cm}^{-2}$ , OFT90% and OFT95% maintained an EU of around 75%, whereas the FT configuration achieved only about 30%. This highlights a significant improvement in electrolyte utilization capability offered by the optimized PEs compared to conventional PEs.

These advantages directly contribute to higher energy density. For instance, under Q3-I150 conditions, the energy density

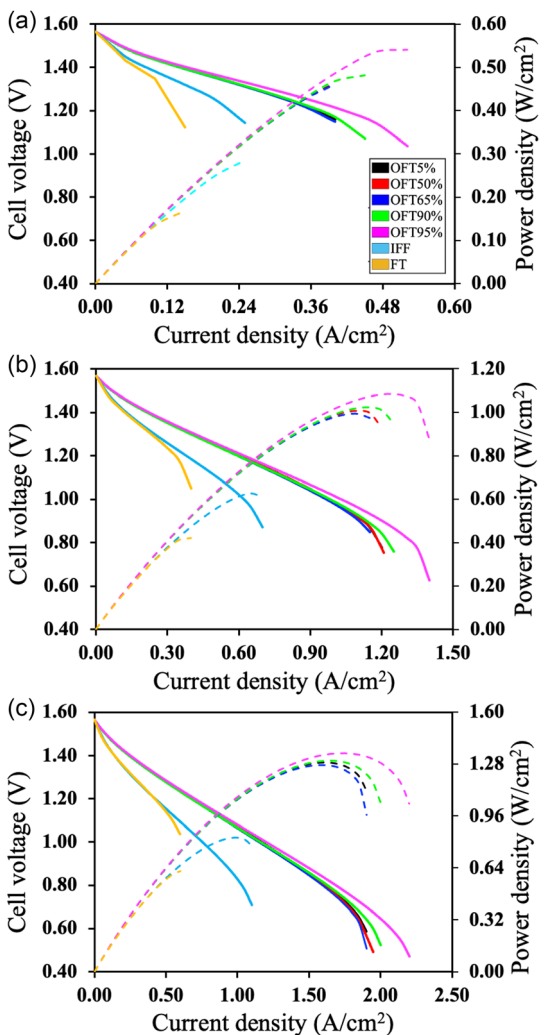


**Figure 5.** Comparison among FT, IFF, OFT5%, OFT50%, OFT65%, OFT90%, and OFT95% using polarization curves at 5% DoD at volumetric electrolyte flow rate for a) 1  $\text{mL min}^{-1}$ , b) 3  $\text{mL min}^{-1}$ , and c) 5  $\text{mL min}^{-1}$ .

of the OFT95% configuration reached 42.6  $\text{Wh L}^{-1}$  of electrolyte, compared to just 15.37  $\text{Wh L}^{-1}$  for the FT configuration. To deliver 1 MWh of energy in a large-scale storage application, the OFT95% would require  $\approx 23,500 \text{ L}$  of electrolyte per half-cell, whereas the FT design would need up to 65,000 L. Therefore, the OFT95% design can significantly reduce the required electrolyte volume by about 60% compared to the conventional FT design. Notably, the differences in utilization among configurations diminished at higher flow rates, where mass transport losses were minimized during operation at 50  $\text{mA cm}^{-2}$ . It is also noteworthy that at a high current density of 150  $\text{mA cm}^{-2}$  and a low volumetric flow rate of 1  $\text{mL min}^{-1}$ , the EU of OFT90% and OFT95% remained comparable at more than 40% (see at Figure 7), while OFT5%, OFT50%, and OFT65% exhibited slightly lower performance. This highlights that OFT90% and OFT95% are more effective under extreme operating conditions—characterized by limited electrolyte flow and high current demand—where mass transport limitations are significant and the availability of active species becomes critical.

To better understand how a heterogeneous electrode structure enhances cell performance, as well as the factors leading to differences in optimized designs at various optimization points, we analyzed transport behaviors within the design domains. Figure 8 shows the distribution of the mass transfer coefficient and velocity vectors within the design domain for each case in this study. Since the flow-through cell design uses PE directly aligned from inlet to outlet, the electrolyte flows directly across, creating uniform but limited mass transport. In contrast, The OFTs contain interdigitated-like channels within the electrode that significantly alter electrolyte flow paths. As shown in Figure 8, these optimized paths enhance performance by directing the flow through high porosity regions with greater ease, increasing both velocity and mass transfer coefficients. Consequently, in the OFTs, electrolyte flow is not strictly vertical as in the FT but follows paths that reduce resistance, facilitate mass transport, and improve access to reactive surfaces with unique pathway of electrolyte flows. In the high-porosity areas, the electrolyte flows more readily, achieving higher velocities and enhanced mass transfer. This contrasts with the low-porosity areas, where increased material density supports electron transfer and offers a larger active surface area for electrochemical reactions. However, reducing porosity in some regions restricts mass transport and may lead to a “starving” effect in terms of chemical species availability. In the context of VRFB operation during discharge, this mass refers primarily to divalent vanadium ions ( $\text{V}^{2+}$ ) in the negative electrode and pentavalent vanadium ions ( $\text{V}^{5+}$ ) and protons ( $\text{H}^+$ ) in the positive electrode. Thus, balancing active surface area and access to reactant species is essential for optimizing porous electrode performance. This balance supports effective reaction rates and minimizes transport limitations, leading to a high-performance electrode structure that can accommodate the electrolyte and electron transport demands across various operational conditions.

An intriguing point in the optimized designs is the formation of interdigitated-like channels specifically in the positive electrode, where the diffusivity of vanadium ions and reaction rate constant are higher than in the negative electrode. This pattern likely emerges due to proton transport limitations within the system. In the VRFB reaction, the negative electrode does not require protons. However, in the positive electrode, where two protons are essential to complete the reaction, proton availability becomes a key factor. Although proton diffusivity is relatively high, the reaction's demand for two protons makes the positive electrode reliant on an efficient proton supply. Additionally, the viscosity of the positive electrolyte is about twice that of the negative electrolyte, reducing its flow velocity within similar porosity conditions. Consequently, the interdigitated-like channels in the positive electrode should facilitate better proton access. Proton supply to the reaction zone occurs through two main pathways: first, from the electrolyte reservoir via the inlet, and second, by proton transport across the membrane. The channels close to the membrane help draw protons to reaction sites, especially at the distal regions of the electrode. An equally compelling observation is why these interdigitated channels form in the negative electrode as seen in all OFT designs. The difference lies in

*Operating current density*

## Volumetric electrolyte flow rate

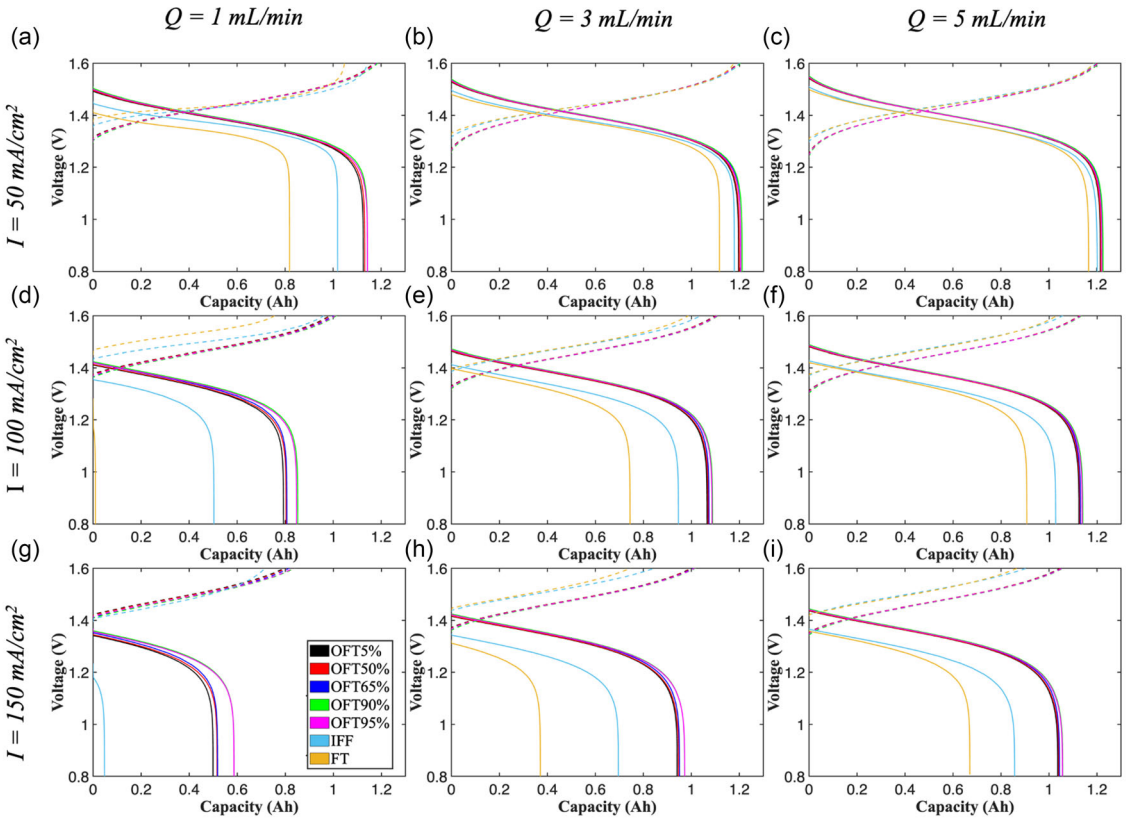


**Figure 6.** Charge and discharge curves at various volumetric electrolyte flow rates while operating at current density a–c)  $50 \text{ mA cm}^{-2}$ , d–f)  $100 \text{ mA cm}^{-2}$ , and g–i)  $150 \text{ mA cm}^{-2}$ .

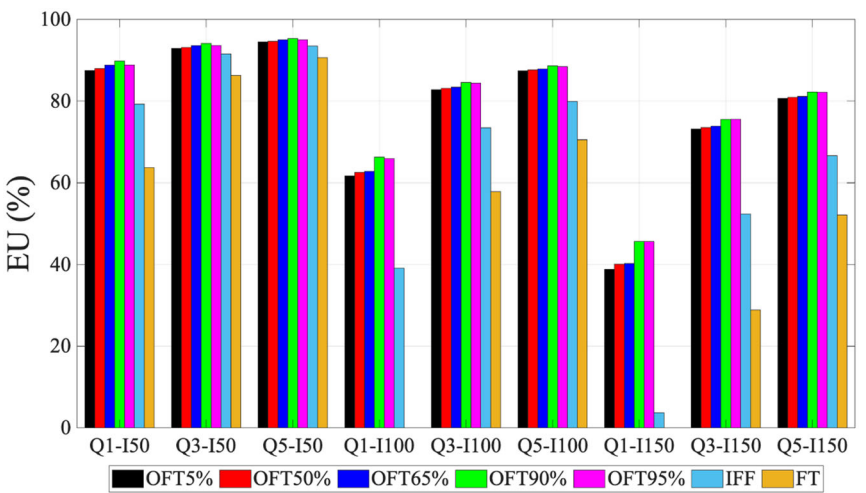


**Figure 7.** Electrolyte utilization during discharge at various current densities and volumetric electrolyte flow rates (e.g., Q1-I150 refers to operating at an electrolyte flow rate of  $1 \text{ mL min}^{-1}$  and current density of  $50 \text{ mA cm}^{-2}$ ).

the diffusivity of vanadium ions and the reaction rate constant, which are relatively low in the negative electrode. Under low material availability, as seen in high DoD conditions, a tradeoff

is necessary: reducing the material at the inlet forms a channel that allows the reactant to travel efficiently toward the farthest end. This setup maximizes the utilization of the design domain,

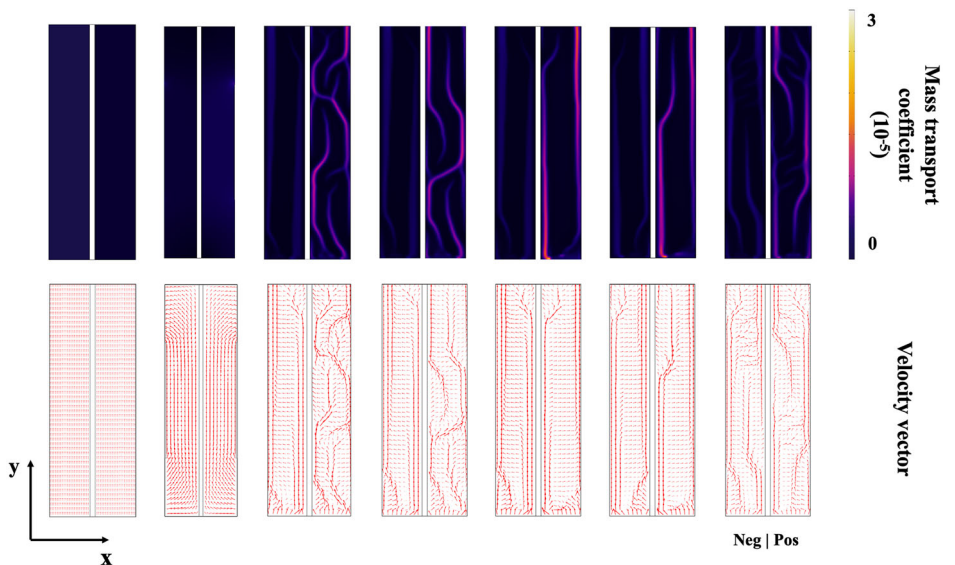


**Figure 8.** Mass transfer coefficient within the calculated domains at an electrolyte flow rate of  $3 \text{ mL min}^{-1}$ , including velocity vectors, with vector lengths indicating velocity magnitude.

ensuring that the entire structure contributes to the reaction, particularly when reactant concentrations are limited. Thus, channel formation, particularly interdigitated channels, optimizes the flow path and reactant availability, ensuring that both the positive and negative electrodes perform effectively under their respective conditions and reactant limitations.

Figure 9 illustrates the distribution of reactant concentration, proton concentration, electrochemical reaction rate, and overpotential for both electrodes across all considered cases operating at a current density of  $100 \text{ mA cm}^{-2}$  and an electrolyte flow rate of  $3 \text{ mL min}^{-1}$ . Notably, the fixed current density ensures a fair comparison, as it establishes that the reactant consumption rate remains consistent across cases. Examining the reactant concentration and proton concentration, the FT cell design shows a depletion of reactants over the path length within the PE, resulting in a lower average concentration than the IFF. This is due to the flow characteristics of the IFF cell design, where convective force under the rib regions promotes concentrated reactant delivery to the porous domains. The IFF's flow pattern enhances reactant transport but still suffers from nonoptimal channel geometry, which can hinder electrochemical kinetics, as previously reported.<sup>[42]</sup> The unoptimized channel configuration results in an uneven reaction rate distribution, creating regions with lower reaction activity and producing an overpotential profile similar to that of the FT design. Although the reaction rate in the FT design is more uniform than in the IFF configuration, the reactant facilitation from convective forces is weaker. This affects the mass transfer coefficient, which represents the efficiency of chemical species transfer from the bulk electrolyte to the electrode surface. As a result, the limited transfer of chemical species to the electrode surface for electrochemical reactions leads to higher overpotential magnitudes, despite the uniform reaction rate. The convective force advantage in the IFF is particularly beneficial at higher current densities when concentration

gradients increase, making mass transport more challenging. In contrast, the topologically optimized PEs show distinct advantages, especially with the heterogeneous structures. Notably, the OFT95% design, which features unique interdigitated-like channels in the negative electrode, enables efficient reactant and proton supply even to the farthest points within the domain. This results in a more favorable concentration profile compared to the IFF. Although FT shows the most uniform reaction rate distribution among the designs, its overpotential remains significantly higher, likely due to a lower mass transfer coefficient that limits the surface concentration. The structured channeling in the optimized designs, especially in the OFT95%, mitigates overpotential at both negative and positive PEs, including improving the uniformity of reactant and proton distribution even compared among optimized PEs, making these configurations highly effective for enhancing VRFB performance at various operating conditions.

While the optimized PE design has shown superior performance, particularly in maximizing electrolyte utilization due to its ability to manage low-concentration reactants, there remains a critical consideration for real-world applications that has yet to be addressed: hydraulic power loss. The increased material density and lower porosity of the optimized PE design inevitably led to higher hydraulic resistance, which raises operational energy costs for the system. However, whether this tradeoff is beneficial overall is still uncertain. To assess this, we evaluated each design for energy efficiency and hydraulic energy loss, ultimately calculating the round-trip efficiency to provide a basis for design recommendations. Since each configuration varies in its operational capability (e.g., some can handle discharge at  $1 \text{ A cm}^{-2}$  while others cannot), energy efficiency was analyzed across a range of discharge current densities tailored to each case's capacity. Figure 10a presents the energy efficiency of each design across a range of discharging current densities from 50, 100, and

$150 \text{ mA cm}^{-2}$  under various operating conditions. At low current densities, all designs performed similarly, achieving  $\approx 80\%$  energy efficiency or even reach 90% at higher flow rates—except for the FT configuration when the electrolyte was fed at  $1 \text{ mL min}^{-1}$ . However, at higher current densities, the energy efficiency of homogeneous electrodes declined sharply, indicating that their simple structures struggle under increased demand. The optimized PE achieves a notable more than 40% efficiency even at higher current density of  $150 \text{ mA cm}^{-2}$  and a low volumetric flow rate of  $1 \text{ mL min}^{-1}$ . Moreover, the OFT90% and OFT95% configurations exhibit slightly higher energy efficiency among

the optimized PEs, representing an advantage of topologically optimized structures under reactant-starved conditions, whereas the conventional FT configuration cannot operate under such conditions.

Figure 10b shows the hydraulic energy loss across different flow rates. Among the optimized designs, OFT65% and OFT90% required the highest hydraulic energy, while OFT95% remained competitive with OFT5% and OFT50%, despite achieving higher performance. This difference is due to the structural variations where high-density regions at inlet and entire domains in the OFT65% and OFT90% create more resistance, increasing the

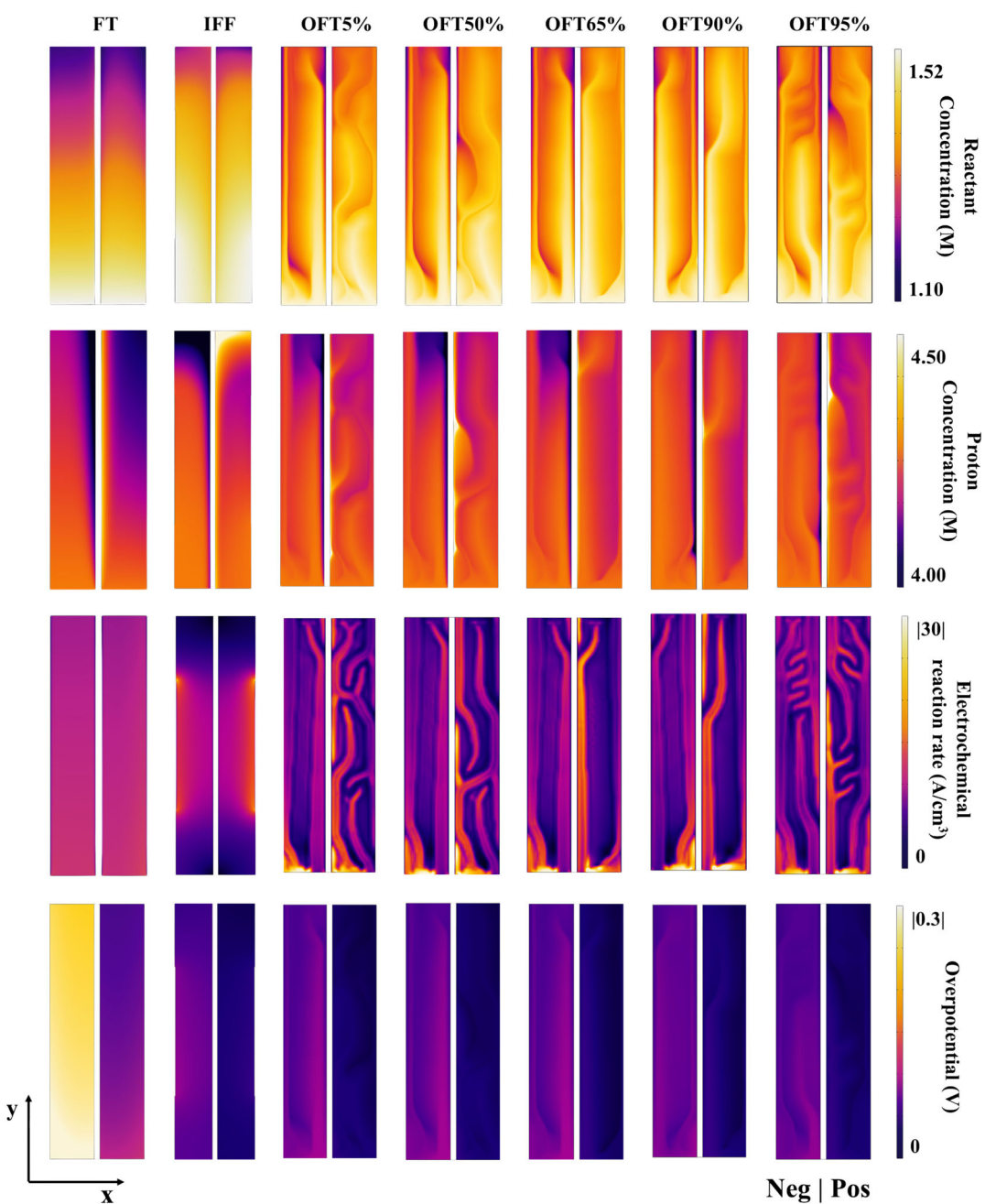


**Figure 9.** Comparison of reactant concentration, rate of reaction, proton concentration, and overpotential distribution from top to bottom among FT, IFF, OFT5%, OFT50%, OFT65%, OFT90%, and OFT95% at a fixed flow rate of  $3 \text{ mL min}^{-1}$  and a current density of  $0.1 \text{ A cm}^{-2}$  while operating at 5% DoD.

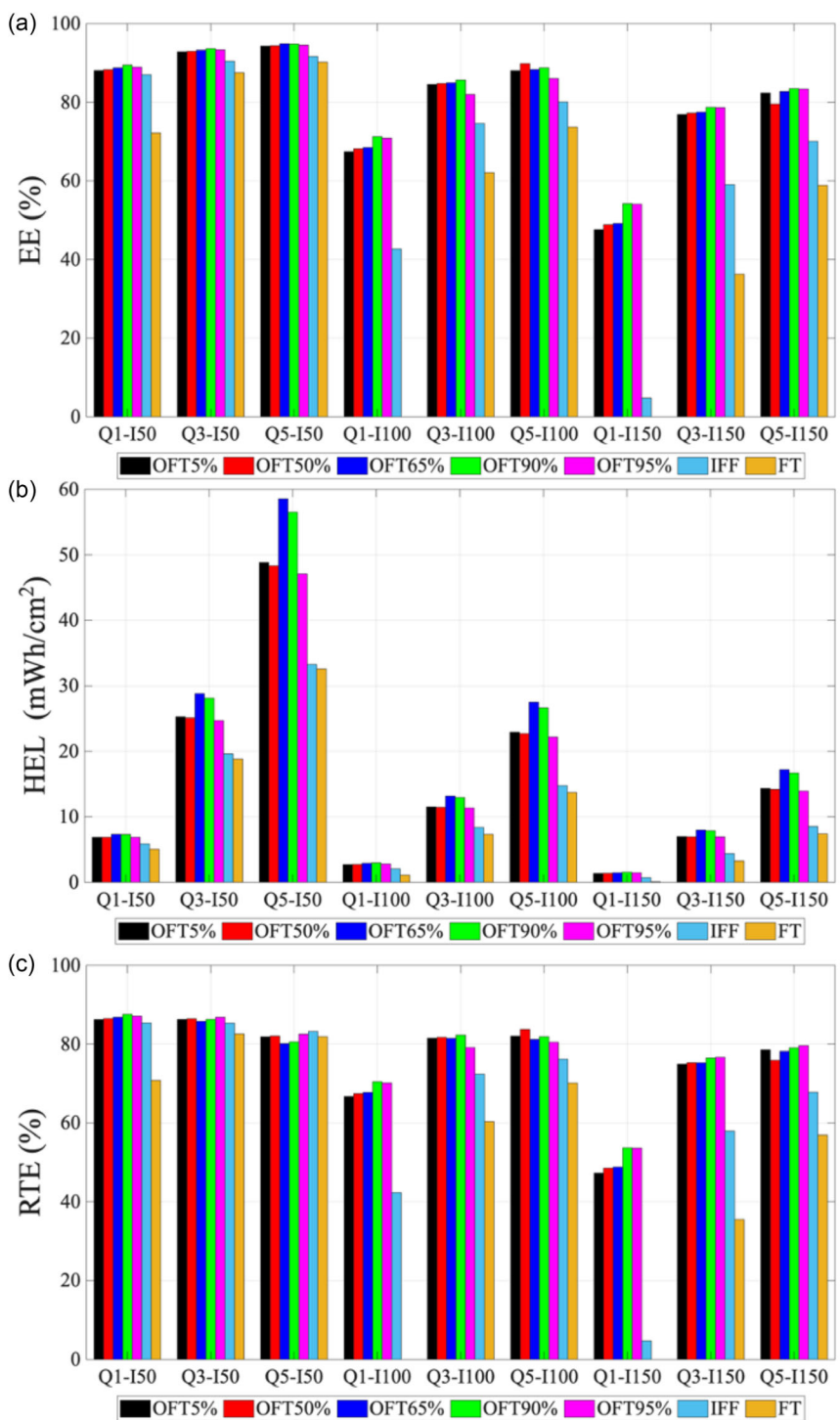


**Figure 10.** Comparison of a) energy efficiency of FT, IFF, OFT5%, OFT50%, OFT65%, OFT90%, and OFT95% during operation at various current densities and volumetric electrolyte flow rates; b) hydraulic energy loss across different types of porous electrodes, including cell designs, as electrolyte flows through the porous electrode domain at volumetric flow rates of 1, 3, and 5 mL min<sup>-1</sup>, representing the rated flow rates for a small-scale flow cell; c) round-trip efficiency of FT, IFF, OFT5%, OFT50%, OFT65%, OFT90%, and OFT95% during operation at various current densities and volumetric electrolyte flow rates.

power required for electrolyte flow (see Figure 3f). These hydraulic energy loss were then incorporated to calculate the round-trip efficiency of each design. The optimized PEs operating at flow rates of 1, 3, and 5 mL min<sup>-1</sup> and a current density of 50 mA cm<sup>-2</sup> exhibit similar performance compared to the unmodified PEs of

IFF. However, at higher current densities, the performance gap between the optimized and unmodified PEs of IFF becomes relatively larger, particularly under conditions of high current density and low flow rate. Under these conditions, OFT90% and OFT95% are more suitable than the other optimized PEs

due to their flow characteristics, as discussed earlier, which mitigate reactant depletion at high current density. This highlights the effectiveness of topology-optimized PE structures in enhancing performance. The advancement of heterogeneous structures enables further improvement of overall performance, especially at lower flow rates, contributing to the reduction of hydraulic energy losses. Furthermore, operation at higher current densities supports VRFB system design by lowering battery stack costs, as the implementation of high-performance single cells reduces the number of cells required to achieve a specific rated power. Notably, at low flow rates, the FT structure showed lower round-trip efficiency compared to the IFF, but as the flow rate increased, the FT surpassed the IFF in round-trip efficiency, reflecting its better response to higher electrolyte velocities. The comparison round-trip efficiency for each cell design is illustrated in Figure 10c.

Considering all aspects of performance, the OFT95% emerges as the most recommended design due to the following reasons: 1) High current density capability: The OFT95% can deliver high current densities of up to  $2.2 \text{ A cm}^{-2}$  when needed, making it ideal for applications that require quick responses to power demands. 2) Maximized capacity and electrolyte utilization: Although OFT90% and OFT95% exhibit comparable charge/discharge capacities, OFT95% remains the most competitive design—particularly under high current density and low flow rate conditions. Among all OFT configurations, OFT95% delivers the most effective performance by optimizing electrolyte utilization, thereby enhancing the energy density of the VRFB without necessitating major modifications to other system components. 3) Greater round-trip efficiency: Although its round-trip efficiency is comparable with the other optimized electrodes at low current density, however, the OFT95% show a superior RTE when operate at higher current densities, demonstrating compatibility with high efficiency system operation while using OFT 95%.

The optimized electrode structure achieved in this study underscores the substantial performance gains achievable by implementing interdigitated-type channels within porous electrodes for a flow-through cell design. This configuration notably enhances cell performance, surpassing the traditional IFF in key metrics, such as electrolyte utilization, current density response, and capacity. Nevertheless, practical challenges in fabricating such intricate electrode structures persist, necessitating innovative approaches to integrate these designs into real-world applications. To address these challenges, we propose several feasible fabrication pathways. First, rather than replicating the intricate 2D root-like channels, it may be more practical to focus on recreating the projected porosity distributions observed in Figure 4a-d. This approach could involve constructing multilayer porous electrodes, each layer tailored with distinct porosities to emulate the desired structure within a scalable, manufacturable stack design. Alternatively, large voids (channels) could be incorporated directly into the electrode through processes like molding and stamping<sup>[18,19]</sup> and electrode modifications.<sup>[6,7]</sup> A more advanced approach is to employ nanoscale 3D printing to precisely print the electrode structure, followed by carbonization to achieve optimal electrochemical properties. This method holds promise

for achieving the fine-scale control needed for customized porous designs, allowing us to retain structural integrity while achieving high-performance characteristics. Ongoing research within our group continues to explore and refine these fabrication techniques, focusing on balancing manufacturability with performance gains. Our efforts aim to translate these optimized electrode architectures into scalable solutions that further the development of high-efficiency flow-through systems.

## 4. Conclusions

This study successfully demonstrated the impact of optimized PE structures on enhancing the performance of VRFBs, particularly when operating in FT cell configurations. Using a comprehensive TO approach that considers proton transport, species diffusion, electrolyte flow, and reaction kinetics within both positive and negative electrodes, we achieved significant improvements in energy efficiency and power density. The inclusion of interdigitated-type channels within the optimized electrodes not only facilitated enhanced mass transport but also supported more uniform reactant distribution, mitigating the concentration gradients that commonly limit performance in traditional designs. Performance evaluations, including polarization and charge/discharge tests, confirmed that the optimized electrodes outperformed conventional FT and IFF structures, with the OFT95% design proving particularly effective in maximizing electrolyte utilization under low reactant conditions. Although the optimized structures exhibited increased hydraulic power loss due to lower porosity, this tradeoff was minimal, and the round-trip efficiency remained competitive and even higher when operate at higher current densities. The results underscore the necessity of balancing active surface area with mass transport pathways to achieve high-performance VRFBs. This study advances the understanding of electrode architecture for VRFBs and sets a foundation for further research on sustainable, high-efficiency energy storage solutions, contributing to the broader goal of carbon neutrality.

## Acknowledgements

This research project is supported by King Mongkut's University of Technology Thonburi (KMUTT), Thailand Science Research and Innovation (TSRI), and National Science, Research and Innovation Fund (NSRF) Fiscal year 2026.

## Conflict of Interest

The authors declare no conflict of interest.

## Author Contributions

**Poramet Aiemsathit:** formal analysis (lead); investigation (lead); methodology (lead); software (lead); validation (lead); visualization (lead); writing—original draft (lead). **Mehrzed Alizadeh:** formal

analysis (supporting); software (supporting); writing—review and editing (supporting). **Yossapong Laounual:** formal analysis (supporting); writing—review and editing (supporting). **Patcharawat Charoen-amornkitt:** conceptualization (lead); formal analysis (lead); funding acquisition (lead); methodology (supporting); project administration (lead); resources (lead); software (supporting); supervision (lead); writing—review and editing (lead). **Takahiro Suzuki:** formal analysis (supporting); software (supporting); writing—review and editing (supporting). **Shohji Tsushima:** formal analysis (supporting); software (supporting); writing—review and editing (supporting).

## Data Availability Statement

Research data are not shared.

**Keywords:** numerical modeling • porous electrodes • topology optimization • vanadium redox flow batteries

- [1] U.S. Environmental Protection Agency (EPA), *Inventory of U.S. Greenhouse Gas Emissions and Sinks: 1990–2022*, U.S. Environmental Protection Agency, Washington, D.C. 2024, EPA.gov, April 11, [Online], <https://www.epa.gov/ghgemissions/inventory-us-greenhouse-gas-emissions-and-sinks>.
- [2] K. Nantasaksiri, P. Charoen-amornkitt, T. Machimura, *Renewable Sustainable Energy Transition* 2021, 1, 100011.
- [3] J. Mitali, S. Dhinakaran, A. A. Mohamad, *Energy Storage Sav.* 2022, 1, 166.
- [4] W. Wang, B. Yuan, Q. Sun, R. Wennersten, *J. Energy Storage* 2022, 52, 104812.
- [5] J. Noack, L. Wietschel, N. Roznyatovskaya, K. Pinkwart, J. Tübke, *Energies* 2016, 9, 627.
- [6] I. Mayrhuber, C. R. Dennison, V. Kalra, E. C. Kumbur, *J. Power Sources* 2014, 260, 251.
- [7] A. Bhattachari, N. Wai, R. Schweiss, A. Whitehead, T. M. Lim, H. H. Hng, *J. Power Sources* 2017, 341, 83.
- [8] L. Eifert, R. Banerjee, Z. Jusys, R. Zeis, *J. Electrochem. Soc.* 2018, 165, A2577.
- [9] V. Kiniman, C. Kanokwhale, P. Boonto, W. Pholauyphon, K. Nantasaksiri, P. Charoen-amornkitt, T. Suzuki, S. Tsushima, *J. Energy Storage* 2024, 83, 110804.
- [10] N. Limjeerajarus, P. Charoen-amornkitt, *Int. J. Hydrogen Energy* 2015, 40, 7144.
- [11] C. R. Dennison, E. Agar, B. Akuzum, E. C. Kumbur, *J. Electrochem. Soc.* 2015, 163, A5163.
- [12] B. Akuzum, Y. C. Alparslan, N. C. Robinson, E. Agar, E. C. Kumbur, *J. Appl. Electrochem.* 2019, 49, 551.
- [13] L. Wei, Z. X. Guo, J. Sun, X. Z. Fan, M. C. Wu, J. B. Xu, T. S. Zhao, *Int. J. Heat Mass Transfer* 2021, 179, 121747.
- [14] F. Yang, L. Fan, Y. Chai, Y. Zheng, D. Qu, *J. Energy Storage* 2023, 67, 107683.
- [15] Y. Chai, D. Qu, L. Fan, Y. Zheng, F. Yang, *J. Energy Storage* 2024, 78, 110278.
- [16] Q. Xu, T. S. Zhao, P. K. Leung, *Appl. Energy* 2013, 105, 47.
- [17] Z. Guo, J. Sun, Z. Wang, X. Fan, T. Zhao, *Int. J. Heat Mass Transfer* 2023, 201, 123548.
- [18] M. Watanabe, H. Yanai, M. Nasu, *J. Electrochem. Soc.* 2019, 166, F3210.
- [19] T. Inoue, D. Sakai, K. Hirota, K. Sano, M. Nasu, H. Yanai, M. Watanabe, M. Uchida, *J. Electrochem. Soc.* 2022, 169, 114504.
- [20] M. Alizadeh, P. Charoen-Amornkitt, T. Suzuki, S. Tsushima, *Prog. Energy* 2024, 7, 012003.
- [21] L. L. Beghini, A. Beghini, N. Katz, W. F. Baker, G. H. Paulino, *Eng. Struct.* 2014, 59, 716.
- [22] J.-H. Zhu, W.-H. Zhang, L. Xia, *Arch. Comput. Methods Eng.* 2016, 23, 595.
- [23] V. Wanittansirichok, K. Mongkolphan, N. Chaowalitbumrung, Y. Sukjai, P. Promoppatum, *J. Energy Storage* 2022, 55, 105703.
- [24] S. Waelveerakup, K. Thanomthong, P. Tantivimonkajorn, V. Wanittansirichok, K. Mongkolphan, K. Sakamatapan, P. Promoppatum, S. Wongwises, *Energy* 2024, 298, 131364.
- [25] C. Q. Wu, C. Yang, Q. Xiao, H. B. Ke, H. J. Xu, *Int. J. Therm. Sci.* 2022, 181, 107771.
- [26] M. Alizadeh, P. Charoen-amornkitt, T. Suzuki, S. Tsushima, *J. Electrochem. Soc.* 2023, 170, 114520.
- [27] M. Alizadeh, P. Charoen-amornkitt, T. Suzuki, S. Tsushima, *Chem. Eng. Sci.* 2023, 275, 118739.
- [28] P. Charoen-amornkitt, M. Alizadeh, T. Suzuki, S. Tsushima, *Int. J. Heat Mass Transfer* 2023, 202, 123725.
- [29] M. Alizadeh, P. Charoen-amornkitt, T. Suzuki, S. Tsushima, *Energy Convers. Manage.* 2023, 294, 117567.
- [30] M. Long, M. Alizadeh, P. Charoen-amornkitt, T. Suzuki, S. Tsushima, *Chem. Eng. Sci.* 2024, 298, 120420.
- [31] R. Behrou, A. Pizzolato, A. Forner-Cuenca, *Int. J. Heat Mass Transfer* 2019, 135, 72.
- [32] C. Qu, Y. Zhang, Z. Zhang, M. Zheng, *Processes* 2023, 11, 2482.
- [33] Y. Xia, C. Guo, E. Dong, L. Chen, W. Tao, *Int. J. Heat Mass Transfer* 2024, 222, 125147.
- [34] P. Passakornjaras, P. Orncompa, M. Alizadeh, P. Charoen-amornkitt, T. Suzuki, S. Tsushima, *J. Electrochem. Soc.* 2024, 171, 074502.
- [35] K. Yaji, S. Yamasaki, S. Tsushima, T. Suzuki, K. Fujita, *Struct. Multidiscip. Optim.* 2018, 57, 535.
- [36] T. Y. Lin, S. E. Baker, E. B. Duoss, V. A. Beck, *J. Electrochem. Soc.* 2022, 169, 050540.
- [37] C.-H. Chen, K. Yaji, S. Yamasaki, S. Tsushima, K. Fujita, *J. Energy Storage* 2019, 26, 100990.
- [38] T. Roy, M. A. S. de Troya, M. A. Worsley, V. A. Beck, *Struct. Multidiscip. Optim.* 2022, 65, 171.
- [39] V. A. Beck, J. J. Wong, C. F. Jekel, D. A. Tortorelli, S. E. Baker, E. B. Duoss, M. A. Worsley, *J. Power Sources* 2021, 512, 230453.
- [40] H. Li, G. Bucci, N. W. Brady, N. R. Cross, V. M. Ehlinger, T. Y. Lin, M. A. S. de Troya, D. Tortorelli, M. A. Worsley, T. Roy, *Struct. Multidiscip. Optim.* 2024, 67, 188.
- [41] S. Tsushima, T. Suzuki, *J. Electrochem. Soc.* 2020, 167, 020553.
- [42] P. Qian, H. Zhang, J. Chen, Y. Wen, Q. Luo, Z. Liu, D. You, B. Yi, *J. Power Sources* 2008, 175, 613.
- [43] B. S. Lazarov, O. Sigmund, *Int. J. Numer. Methods Eng.* 2011, 86, 765.
- [44] M. Vynnycky, *Energy* 2011, 36, 2242.
- [45] T. Yamamura, N. Watanabe, T. Yano, Y. Shiokawa, *J. Electrochem. Soc.* 2005, 152, A830.
- [46] A. A. Shah, M. J. Watt-Smith, F. C. Walsh, *Electrochim. Acta* 2008, 53, 8087.
- [47] S. Zhu, R. H. Pelton, K. Coliver, *Chem. Eng. Sci.* 1995, 50, 3557.
- [48] K. W. Knehr, E. Agar, C. R. Dennison, A. R. Kalidindi, E. C. Kumbur, *J. Electrochem. Soc.* 2012, 159, A1446.

Manuscript received: January 23, 2025

Revised manuscript received: September 30, 2025

Version of record online: